Causality in the Dual-Fermion Approach

Author
William Skoglund

Supervisor
Erik van Loon
Co-supervisor
Akshat Mishra

Thesis submitted for the degree Master of Theoretical Physics
Project duration: 4 Months

LUND
UNIVERSITY

Department of Physics
Division of Mathematical Physics
May 2026

Acknowledgments

I would like to express my deep gratitude to Erik for the opportunities to work with him over the past two and a half years on various projects. It has been a pleasure to learn more about condensed matter physics with you, and I have especially enjoyed learning about the dual-fermion approach. Thank you for taking the time out of your schedule for our weekly meetings, and for your insightful guidance.

I would also like to thank Akshat for generously taking the time to explain concepts and for the helpful discussions. Your company has always been enjoyable, and I wish you all the best for the remainder of your PhD journey.

Thank you to Emma for your continued support and encouragement throughout the writing of this thesis. I am also grateful to my family for always being supportive.

Lastly, thank you Wilma for the fantastic times throughout the years. You are deeply missed by everyone.

Usage of GAI

Generative AI has been used to polish and format certain parts of the text.

Abstract

Causality is a fundamental requirement for physical consistency in many-body approximations. In the context of Green's functions, causality requires a positive spectral function and analyticity in the upper half of the complex-frequency plane. These properties are not guaranteed by approximate methods, and formal proofs of causality for the underlying approximation schemes are often difficult to establish. The recently rediscovered Nevanlinna–Pick criterion provides a practical way to test causality directly from Matsubara-frequency data, without performing analytic continuation to the real-frequency axis. In this work, we use the Nevanlinna–Pick criterion to investigate the causality of the ladder dual-fermion approach, a diagrammatic extension of dynamical mean-field theory designed to incorporate nonlocal correlations. The analysis is performed for the spinless Falicov–Kimball model, which provides a useful testing ground because several quantities can be computed exactly or semi-analytically, avoiding Monte Carlo noise. This is particularly important since the Nevanlinna–Pick criterion is highly sensitive to noise in the input data. In addition, we derive several analytical properties of the Pick matrix, providing insight into the structure of the criterion when applied to Green's functions. For small systems, apparent causality violations are observed, but these are found to be associated with finite-size effects. For larger system sizes, no robust signs of causality violations are found, neither within the full ladder dual-fermion approach nor within the leading dual-fermion correction.

Contents

1 Introduction **1**

2 Theory **2**
2.1 Conventions and Assumptions . . . 2
2.2 Green's Functions in the Finite Temperature Formalism . . . 2
2.2.1 The Matsubara Green's Function . . . 2
2.2.2 Self-Energy . . . 4
2.2.3 Note on Imaginary Time . . . 4
2.2.4 The Retarded Green's Function and Causality . . . 5
2.3 Analytic Continuation . . . 7
2.3.1 Extracting the Spectral Function from Matsubara Data . . . 7
2.3.2 Nevanlinna Functions . . . 7
2.3.3 The Pick Criterion . . . 8
2.4 Systems . . . 9
2.4.1 The Falicov–Kimball Model . . . 9
2.4.2 The Charge-Density Wave Phase . . . 11
2.4.3 The Anderson Insulating Phase . . . 11
2.4.4 Impurity Models . . . 12
2.5 Dynamical Mean-Field Theory . . . 13
2.5.1 Causality in Dynamical Mean-Field Theory . . . 15
2.6 The Dual-Fermion Approach . . . 15
2.6.1 Derivation of Dual Transformation . . . 15
2.6.2 Dual Relations and Self-Energy . . . 17
2.6.3 The Ladder Approximation . . . 18
2.6.4 Static and Dynamic Scattering . . . 19
2.6.5 Computational Scheme . . . 19
2.6.6 Self-Consistency Conditions . . . 21
2.6.7 Causality in the Dual-Fermion Approach . . . 21

3 Method **22**
3.1 Computational Schemes and Default Parameters . . . 22
3.2 Numerical Aspects of the CDW Phase . . . 23
3.3 Verification of Positive Semidefiniteness . . . 24

4 Results **25**
4.1 Benchmarking Approximation Schemes – 4×4 Systems . . . 25
4.1.1 Comparison with Exact Diagonalization at Half Filling . . . 25
4.1.2 Comparison with Exact Diagonalization away from Half Filling . . . 27
4.1.3 Convergence at Half Filling . . . 28
4.1.4 Convergence of Finite Truncation BSE to Ladder BSE . . . 29
4.2 The Pick Matrix for Causal Systems - Analytical Results . . . 30
4.2.1 Exact Green's Function . . . 30
4.3 Causality in the Dual-Fermion Approach . . . 31

4.3.1 Causality at Half Filling . . . 31
4.3.2 Causality away from Half Filling . . . 33
4.3.3 Finite Truncation of the BSE . . . 35
4.3.4 Effects of Interpolation Node Number on the Pick Eigenvalues . . . 35
4.3.5 Finite Size Effects . . . 37

5 Conclusion **39**

6 Appendix **45**
6.1 Properties of the Pick Matrix . . . 45
6.1.1 Nevanlinna-Pick Matrix . . . 45
6.1.2 Computations for the Pick Matrix of the Exact Green's Function . . . 46
6.1.3 Noninteracting Limit . . . 46
6.2 Additional Results . . . 47
6.2.1 CDW Instability away from Half Filling . . . 47
6.2.2 Finite Truncation of the BSE . . . 48
6.2.3 Parameter-Space Diagrams at $L = 16$ . . . 50

Acronyms

DMFT	–	Dynamical Mean-Field Theory
DF/DFA	–	Dual Fermion/Dual-Fermion Approach
PSD	–	Positive semidefinite
CDW	–	Charge-density wave
ED	–	Exact diagonalization
BSE	–	Bethe-Salpeter equation

Symbols

$\mathbb{C}^+$	–	Upper half-plane, $\{z \mid \mathrm{Im}z > 0\}$
$\bar{\mathbb{C}}^+$	–	Closure of the upper half-plane, $\{z \mid \mathrm{Im}z \geq 0\}$
$\mathcal{D}$	–	Complex unit disk without boundary, $\{z \mid \lvert z\rvert < 1\}$
$\bar{\mathcal{D}}$	–	Closure of the complex unit disk, $\{z \mid \lvert z\rvert \leq 1\}$
`B`	–	The class of Schur functions, $\{f \mid f : \mathcal{D} \to \bar{\mathcal{D}}$ analytic in $\mathcal{D}\}$
`N`	–	The class of Nevanlinna functions, $\{f \mid f : \mathbb{C}^+ \to \bar{\mathbb{C}}^+$ analytic in $\mathbb{C}^+$ and $\mathrm{Im}f(z) \geq 0\}$

1 Introduction

Many physical phenomena in materials, including magnetism and charge ordering, originate from the collective behavior of interacting electrons. Understanding these phenomena is essential not only for explaining the properties of existing materials, but also for guiding the design of new materials for future technologies. In principle, an exact solution of the quantum many-electron problem would allow material properties to be determined exactly from first principles. In practice, however, this problem has been studied for almost a century and remains virtually impossible to solve exactly, due to the large number of electrons in real materials, their quantum nature, and the mutual Coulomb interactions that couple their motion.

Several approaches to the many-electron problem have been developed, including density functional theory [1, 2], which uses the electron density as the fundamental variable, and Green's function methods. Green's functions characterize the propagation of electrons and holes in materials and provide direct access to experimentally measurable quantities, such as electronic excitation spectra. They are also powerful theoretical tools, since they can be used to evaluate expectation values of single-particle operators in thermal equilibrium, as well as the ground-state energy [3].

Obtaining the exact Green's function, however, would require an exact solution of the many-body Hamiltonian, and one must therefore resort to approximations. To be useful, such approximations should i) be sufficiently general to be applicable to a wide range of materials, ii) reproduce measured observables and iii) be physically consistent.

A fundamental requirement for physical consistency is that an approximation respects causality, meaning that a cause precedes its effect. Mathematically, a causal response function must vanish identically before the corresponding external perturbation is applied. This condition imposes strict constraints on the analytic structure of response functions in complex-frequency space. Consequently, causal response functions satisfy nontrivial properties such as the Kramers–Kronig relations, which connect the real and imaginary parts of the response function on the real-frequency axis.

Dynamical mean-field theory (DMFT) was introduced in the late 1980s [4] as a nonperturbative approximation scheme for computing the Green's function in strongly correlated systems dominated by local correlation effects. The approximation is based on mapping the lattice system onto an effective single-site impurity problem, which is solved self-consistently. The resulting impurity self-energy, characterizing the interactions of a system, is then assigned to each lattice site. As a result, nonlocal, or momentum-dependent, effects are neglected, since the impurity problem consists of a single site.

To incorporate nonlocal effects and thereby improve upon the DMFT solution, a diagrammatic extension of DMFT, known as the dual-fermion approach, has been developed [5]. The dual-fermion approach is based on an exact change of variables from the physical lattice electrons to a set of dual fermions, constructed such that a noninteracting system of dual fermions reproduces the DMFT solution. Since the change of variables is exact, approximations enter only through the choice of diagrams included in the perturbative expansion.

Although DMFT is known to be causal [6, 7], no formal proof has yet established the causality of the dual-fermion approach. Proving causality for the dual-fermion calculations requires showing both that the self-consistency condition used in the iterative procedure is causal, and that the chosen diagrammatic approximation respects causality. While certain conditions in diagrammatic perturbation theory ensure nonnegative spectral functions, causality is not in general guaranteed for diagrammatic extensions of DMFT [8].

At finite temperature, Green's functions are conveniently expressed within the Matsubara formalism [3], where quantities are evaluated in imaginary time. In this formalism, the Green's function is computed on a discrete set of points along the imaginary-frequency axis. Recovering the physical real-frequency Green's function requires analytic continuation from the imaginary-frequency to the real-frequency axis, where causality can be examined directly.

A recent breakthrough in analytic continuation [9] interpolates the imaginary-frequency data using causal functions, thereby guaranteeing that the resulting real-frequency Green's function is causal whenever such an interpolation is possible. The existence of a causal interpolant can be verified through the Pick criterion [10, 11], which depends only on the input data on the imaginary-frequency axis. This makes it possible to test causality of an approximation scheme without explicitly performing analytic continuation.

The aim of this work is to investigate causality in the dual-fermion approach using the Pick criterion. This is done in the context of the two-dimensional spinless Falicov–Kimball model, a simplified version of the Hubbard model, in which electrons of opposite spin are represented by two distinct species denoted c and f electrons, with the hopping amplitude of the f electrons set to zero. This leads to several simplifications, including the applicability of Wick's theorem for a fixed f-electron configuration, and the separation of static and dynamic susceptibilities [12, 13]. Moreover, several quantities in the Falicov–Kimball model admit analytical expressions. Consequently, the model can be solved numerically exactly, meaning without Monte Carlo noise, making it a suitable testing ground for approximation schemes and their properties.

2 Theory

2.1 Conventions and Assumptions

Natural units are used throughout this work. We consider two-dimensional, time-independent, translationally invariant lattice systems at finite temperature in the grand-canonical ensemble. Additional degrees of freedom, such as spin, are neglected, meaning that the Green's functions are scalar quantities.

2.2 Green's Functions in the Finite Temperature Formalism

2.2.1 The Matsubara Green's Function

Green's functions characterize the propagation of electrons and holes in many-body systems. They provide a means of expressing expectation values of single-particle operators, and their

Fourier transforms contain the one-particle excitation energies associated with electron addition and removal. At finite temperature, it is convenient to work in imaginary time, τ, where the Matsubara Green's function is defined as [3]

$$G_{ij}(\tau) = -\langle \mathcal{T}\hat{c}_i(\tau)\hat{c}_j^\dagger\rangle = -\langle \hat{c}_i(\tau)\hat{c}_j^\dagger\rangle\,\Theta(\tau) + \langle \hat{c}_j^\dagger\hat{c}_i(\tau)\rangle\,\Theta(-\tau). \tag{2.1}$$

Here, $\langle ...\rangle = \frac{1}{Z}\mathrm{Tr}(e^{-\beta\hat{H}}\dots)$ denotes the thermal expectation value in the grand-canonical ensemble, where Z is the partition function, β is the inverse temperature and $\hat{H}$ is the grand-canonical Hamiltonian. Moreover, $\mathcal{T}$ denotes the imaginary-time-ordering symbol, and $\hat{c}, \hat{c}^\dagger$ are the fermionic annihilation and creation operators. The indices i and j label the lattice sites, and $\Theta(\tau)$ is the Heaviside function. Operators are defined in the modified Heisenberg picture,

$$\hat{c}_i(\tau) = e^{\hat{H}\tau}\hat{c}_i e^{-\hat{H}\tau} \quad , \quad \hat{c}_i^\dagger(\tau) = e^{\hat{H}\tau}\hat{c}_i^\dagger e^{-\hat{H}\tau}, \tag{2.2}$$

meaning $[\hat{c}_i(\tau)]^\dagger \neq \hat{c}_i^\dagger(\tau)$ if τ is taken as real. As the Hamiltonian is assumed to be time-independent, the Matsubara Green's function in Eq. (2.1) depends only on one imaginary time variable, in which it is antiperiodic, with period determined by the inverse temperature β [14],

$$G_{ij}(\tau) = -G_{ij}(\tau+\beta) \quad , \quad -\beta < \tau < 0. \tag{2.3}$$

By considering the antiperiodic continuation of the Matsubara Green's function from its fundamental interval $G(\tau), \tau \in (-\beta, \beta)$ to the entire imaginary time axis $\tau \in (-\infty, \infty)$ [15, 16], its Fourier expansion is given by [14]

$$G_{ij}(\tau) = \frac{1}{\beta}\sum_n e^{-\mathrm{i}\nu_n\tau}G_{ij}(\nu_n) \quad , \quad G_{ij}(\nu_n) = \int_0^\beta d\tau\; e^{\mathrm{i}\nu_n\tau}G_{ij}(\tau), \tag{2.4}$$

where $\nu_n = (2n+1)\pi/\beta$ are fermionic Matsubara frequencies[1]. These coincide with the poles of the Fermi-Dirac distribution, each with unit residue [3]. For systems with translational symmetry, the Matsubara Green's function depends only on the relative separation of spatial coordinates, $i-j$, and subsequently on a single momentum $\mathbf{k}$ when Fourier transformed [17]. Evaluating the integral in Eq. (2.4) and performing a Fourier transform in the relative separation yields the Källén-Lehmann representation of the Matsubara Green's function

$$G(\mathbf{k},\nu) = \sum_{mn} |\,\langle\Psi_m|\,\hat{c}_{\mathbf{k}}\,|\Psi_n\rangle\,|^2 \frac{\rho_n + \rho_m}{\mathrm{i}\nu - \omega_{nm}} \quad , \quad \rho_n = \frac{e^{-\beta E_n}}{Z}. \tag{2.5}$$

Here, $|\Psi_m\rangle$ denotes a simultaneous eigenstate of the grand-canonical Hamiltonian and the discrete translation operator associated with translations on the Bravais lattice. The corresponding energy eigenvalue is denoted by E_m,[2] and we define the transition energy as

[1] The integer index n will often be omitted for brevity.

[2] The energy associated with particle number is contained in E_m. Equivalently, if the grand-canonical Hamiltonian is written as $\hat{H} = \hat{h} - \mu\hat{N}$, then $E_m = \varepsilon_m - \mu N_m$.

$\omega_{nm} = E_n - E_m$. Note that $|\Psi_n\rangle$ must be an $N_n = (N_m + 1)$-particle state for the matrix elements to be nonzero. Introducing the spectral function [14]

$$A(\mathbf{k}, \omega) = \sum_{mn} a_{mn}(\mathbf{k})\delta(\omega - \omega_{nm}) \quad , \quad \int_{-\infty}^{\infty} d\omega \; A(\mathbf{k}, \omega) = 1, \tag{2.6}$$

with spectral weights $a_{mn}(\mathbf{k}) = |\langle \Psi_m | \hat{c}_{\mathbf{k}} | \Psi_n \rangle|^2 (\rho_n + \rho_m)$, the Matsubara Green's function can be expressed as

$$G(\mathbf{k}, \nu) = \int_{-\infty}^{\infty} d\omega' \; \frac{A(\mathbf{k}, \omega')}{\mathrm{i}\nu - \omega'}. \tag{2.7}$$

Physically, the spectral function is a probability distribution describing the probability of adding or removing an electron with energy ω [17]. By construction, the spectral function is nonnegative. This follows because, at $\tau = 0$, the operator pairs appearing in the definition of the Green's function are Hermitian conjugates of one another.

2.2.2 Self-Energy

The Matsubara Green's function can be expressed in terms of its noninteracting value, $G_0(\mathbf{k}, \nu)$, through the self-energy, $\Sigma(\mathbf{k}, \nu)$, defined by the Dyson equation [3]

$$G = G_0 + G_0 \Sigma G \iff \Sigma = G_0^{-1} - G^{-1}. \tag{2.8}$$

Here, all quantities are evaluated at the same point in $(\mathbf{k}, \nu)$-space, omitted for brevity. For the assumptions mentioned in Sec. 2.1, Eq. (2.8) is a scalar equation, meaning the Matsubara Green's function can be written as

$$G(\mathbf{k}, \nu) = \frac{1}{\mathrm{i}\nu - (\varepsilon(\mathbf{k}) - \mu) - \Sigma(\mathbf{k}, \nu)} \quad , \quad G_0(\mathbf{k}, \nu) = [\mathrm{i}\nu - (\varepsilon(\mathbf{k}) - \mu)]^{-1}, \tag{2.9}$$

where $\varepsilon(\mathbf{k}) = -2t[\cos(k_x a) + \cos(k_y a)]$ is the noninteracting dispersion relation for a two-dimensional square lattice with nearest-neighbor hopping. Moreover, t is the hopping amplitude and a the lattice constant, which we set to unity.

The self-energy describes the effects of interactions in the system. It shifts and broadens the spectral peaks associated with excitations already present in the noninteracting limit, while also giving rise to additional excitation modes due to correlation effects [14].

2.2.3 Note on Imaginary Time

The imaginary-time formalism is particularly convenient since the perturbative expansion of the Matsubara Green's function closely resembles the corresponding zero-temperature expansion, and Wick's theorem applies for perturbative calculations in both cases [3, 14]. Moreover, disconnected diagrams cancel in the imaginary-time formalism. However, the spectral function cannot be obtained directly from the Matsubara Green's function, and instead requires analytic continuation to real frequencies [3]. This is further discussed in the following section.

2.2.4 The Retarded Green's Function and Causality

Physical properties of many-body systems, such as excitation energies, are contained in the retarded Green's function, which is defined in real time, t, as

$$\mathrm{i}G_{R,ij}(t) = \langle\{\hat{c}_i, \hat{c}_j^\dagger\}\rangle\,\Theta(t), \tag{2.10}$$

where $\{,\}$ denotes the anticommutator. The retarded Green's function in Eq. (2.10) is said to be causal since it satisfies $G_R(t<0)=0$, due to the Heaviside function. Causality is closely related to analyticity [18];

Definition 1. A function $f:\mathbb{C}\to\mathbb{C}$ is said to be analytic in $\mathcal{C}\subset\mathbb{C}$ if it is complex differentiable at every point in $\mathcal{C}$.

Analytic functions have no poles, or isolated singularities, in their domain of definition and are single-valued there, meaning that the region does not contain branch cuts. Formally, analyticity and causality are related by Titchmarsh's theorem [19, Theorem 95],

Theorem 1 (Titchmarsh's Theorem)**.** Let $L^2(\mathbb{R})$ denote the space of complex-valued square-integrable functions,

$$L^2(\mathbb{R}) = \left\{ f:\mathbb{R}\to\mathbb{C} \;\middle|\; \int_{-\infty}^{\infty} |f(t)|^2\,dt < \infty \right\}. \tag{2.11}$$

Then, a function $f\in L^2(\mathbb{R})$ satisfies $f(t<0)=0$ if and only if its Fourier transform $\mathcal{F}(\omega)$ is the boundary value of a function $F(z)$ analytic in $\mathbb{C}^+$, such that $\mathcal{F}(\omega)\equiv F(\omega+\mathrm{i}\eta)\in L^2(\mathbb{R})$ as a function of ω, where $\eta>0$ is an infinitesimal quantity.

If either of the aforementioned conditions holds, then the Kramers–Kronig relations are implied. Titchmarsh's theorem is reflected in the spectral representation of the retarded Green's function. To make this explicit, we introduce the complex Green's function, $\mathscr{G}:\mathbb{R}^2\times\mathbb{C}\to\mathbb{C}$, defined by

$$\mathscr{G}(\mathbf{k},z) = \int_{-\infty}^{\infty} d\omega'\,\frac{A(\mathbf{k},\omega')}{z-\omega'} = \sum_{mn}\frac{a_{mn}(\mathbf{k})}{z-\omega_{mn}}. \tag{2.12}$$

The retarded Green's function is obtained as the boundary value of $\mathscr{G}(\mathbf{k},z)$ when approaching the real axis from the upper half-plane, $G_R(\mathbf{k},\omega)=\mathscr{G}(\mathbf{k},\omega+\mathrm{i}\eta)$ with $\eta>0$ being an infinitesimal quantity [3]. Note that the complex Green's function is analytic in the entire complex plane except on the real axis, where poles are located at the transition energies ω_{nm} with corresponding spectral weights as residues. Similarly, the retarded Green's function is analytic in the upper-half plane when the real frequency ω is promoted to a complex variable, $G_R(\mathbf{k},z)=\mathscr{G}(\mathbf{k},z+\mathrm{i}\eta)$, as the poles of $\mathscr{G}(\mathbf{k},z)$ are shifted infinitesimally below the real axis.

For poles located a finite distance below the real axis, $z_m = E_m - i\Gamma_m$ with $\Gamma_m>0$, the corresponding spectral feature is no longer a delta peak, but acquires a Lorentzian profile with width set by Γ_m. The inverse width is associated with the lifetime of the excitation. In numerical calculations, a similar Lorentzian broadening is often produced by keeping a

finite value of the positive infinitesimal η, which does not represent an intrinsic lifetime, but rather a numerical artifact. Genuine finite-width poles arise in the quasiparticle description of extended systems and are closely related to the Dyson equation and self-energy described in Sec. 2.2.2 [14].

Using the normalization condition of the spectral function in Eq. (2.6), we obtain the asymptotic form of the complex Green's function,

$$\mathscr{G}(\mathbf{k}, z) \overset{|z|\to\infty}{\approx} \frac{1}{z} \int_{-\infty}^{\infty} d\omega' \; A(\mathbf{k}, \omega') = \frac{1}{z}. \tag{2.13}$$

Hence, the Green's function decays sufficiently fast for its Fourier integral over a semicircular contour in the upper half-plane to vanish as the contour radius tends to infinity[3]. Causality then follows from analyticity.

The retarded and Matsubara Green's functions are both encoded in the complex Green's function, since $\mathscr{G}(\mathbf{k}, i\nu)$ reproduces the Matsubara Green's function according to Eq. (2.7). In this sense, the two Green's functions are closely connected as they are different representations of the same underlying object and share the same spectral function [14]. Hence, the spectral function is a central quantity due to both its physical meaning and its mathematical usefulness. It can be extracted from the retarded Green's function as

$$A(\mathbf{k}, \omega) = -\frac{1}{\pi} \mathrm{Im} G_R(\mathbf{k}, \omega), \tag{2.14}$$

which can be proven using the Sokhotski-Plemelj formula [17]. To summarize, an exact Green's function must satisfy:

(i) Causality: The retarded Green's function is causal, $G_R(t < 0) = 0$.
(ii) Analyticity: The complex Green's function is analytic in $\mathbb{C}^+$. The retarded Green's function is the boundary value when approaching the real axis from $\mathbb{C}^+$, while its values at the Matsubara frequencies reproduce the Matsubara Green's function.
(iii) Nonnegative spectral weights: The spectral function is nonnegative, $A(\mathbf{k}, \omega) \geq 0$, and satisfies the normalization condition in Eq. (2.6).

In the literature, a causal Green's function is frequently defined by having nonnegative spectral weights, which is not equivalent with $G_R(t < 0) = 0$. As a simple example, if G_R is causal with a positive spectral function, $-G^R$ is also causal but with a negative spectral function [5, 21]. Similarly, the spectral function is related to the structure of the Green's function only at the boundary of the real axis according to Eq. (2.14). To determine causality, the analytic structure of the Green's function must be known in the entirety of $\mathbb{C}^+$. In this work, we define a causal Green's function as follows:

Definition 2 (Causal Green's function in frequency space)**.** A Green's function in frequency space is said to be causal if the associated complex Green's function $\mathscr{G}(z)$ is analytic in $\mathbb{C}^+$ and satisfies $\mathrm{Im}\,\mathscr{G}(z) \leq 0$ in $\mathbb{C}^+$ [4].

[3] This follows by Jordan's lemma [20].

[4] The condition $\mathrm{Im}\,\mathscr{G}(z) \leq 0$ in $\mathbb{C}^+$ implies nonnegativity of the spectral function whenever the spectral representation is valid. However, causality is not defined solely in terms of nonnegativity of the spectral function, since the spectral representation in Eq. (2.12) may break down. In such cases, the spectral function may still be nonnegative and $\mathscr{G}(z)$ may still be analytic in $\mathbb{C}^+$, while the Nevanlinna–Pick criterion may fail.

2.3 Analytic Continuation

2.3.1 Extracting the Spectral Function from Matsubara Data

Given a spectral function $A(\mathbf{k},\omega)$, the Matsubara Green's function can be calculated using Eq. (2.7). The inverse problem of recovering the spectral function from a Matsubara Green's function requires analytic continuation, which is fundamentally ill posed [22, 23], meaning that a small change in the input data may generate a completely different spectral function. In addition, the kernel relating the spectral function to the Matsubara Green's functions, $\mathcal{K}(\mathrm{i}\nu,\omega) = (\mathrm{i}\nu - \omega)^{-1}$, decays as $1/|\omega|$ for large $|\omega|$, meaning high frequency features of the spectral function are suppressed, making the inverse problem of obtaining $A(\mathbf{k},\omega)$ ill posed [14, 24].

If analytic continuation of the Matsubara Green's function to the boundary of the real axis can be performed, the retarded Green's function is obtained and the spectral function can be extracted using Eq. (2.14). Methods such as Padé approximations [25] or the maximum entropy method [26] are used to obtain the retarded Green's function from the Matsubara data. In general, the maximum entropy method works for data with noise, whereas the Padé approximation works well for resolving sharp features, but positive spectral functions are not guaranteed [9].

2.3.2 Nevanlinna Functions

A recent breakthrough in the field of analytic continuation uses the Nevanlinna structure of the Green's function [9]. Nevanlinna functions are defined as follows [27, 28]:

Definition 3 (Nevanlinna functions)**.** Let $\bar{\mathbb{C}}^+$ denote the closure of the upper half-plane. A function $f : \mathbb{C}^+ \to \bar{\mathbb{C}}^+$ is said to be a Nevanlinna function if it is analytic in $\mathbb{C}^+$ and has a nonnegative imaginary part there, $\mathrm{Im}f(z) \geq 0, z \in \mathbb{C}^+$. The class of Nevanlinna functions is denoted by $\mathtt{N}$.

The negative complex Green's function in Eq. (2.12) is a Nevanlinna function when restricted to the upper half-plane[5],

$$-\mathscr{G}(\mathbf{k},z) \in \mathtt{N}\ \forall \mathbf{k},\ \ z \in \mathbb{C}^+. \tag{2.15}$$

Analyticity of $\mathscr{G}$ in $\mathbb{C}^+$ is clear from its definition, and its imaginary part can be expressed as

$$\mathrm{Im}[-\mathscr{G}(\mathbf{k},z)] = \int_{-\infty}^{\infty} d\omega' A(\mathbf{k},\omega') \frac{\mathrm{Im}z}{(\mathrm{Re}z-\omega')^2 + [\mathrm{Im}z]^2} \overset{(\mathrm{Im}z>0)}{\geq} 0. \tag{2.16}$$

If it is possible to construct a Nevanlinna interpolant for an approximate Matsubara Green's function, the associated complex Green's function is necessarily analytic in $\mathbb{C}^+$ and the spectral function is guaranteed to be nonnegative by Eqs. (2.14) and (2.16) [9].

The class of Nevanlinna functions is closed under addition and multiplication of positive scalars. That is, if $f(z)$ and $g(z)$ are Nevanlinna functions and a, b are real positive numbers,

[5] Henceforth, references to the Green's function having Nevanlinna structure is understood to mean that its negative has Nevanlinna structure.

then $h(z) = af(z) + bg(z)$ is also a Nevanlinna function. Other nontrivial properties of Nevanlinna functions, such as their integral representations, are elaborated on in Refs. [28, 29, 30].

2.3.3 The Pick Criterion

It is possible to formulate a criterion for the existence of a Nevanlinna interpolant associated with a given finite set of Matsubara points in the upper half-plane[6] [9]. This follows from the Pick criterion, originally formulated as a criterion for the existence of an interpolant in the Schur class for points in the complex unit disk [10, 31, 32],

Definition 4. Let $\mathcal{D}$ denote the complex unit disk and $\bar{\mathcal{D}}$ its closure. A function $f : \mathcal{D} \to \bar{\mathcal{D}}$ is said to be a Schur function if it is analytic in $\mathcal{D}$. The class of Schur functions is denoted by $\mathtt{B}$.

Theorem 2 (The Pick criterion)**.** For a function $f \in \mathtt{B}$ to be determined, let $z_1, \ldots, z_N \in \mathcal{D}$ be distinct interpolation nodes, and let $w_1, \ldots, w_N \in \mathcal{D}$ be target values. The interpolation problem

$$f(z_m) = w_m, \quad m = 1, \ldots, N, \tag{2.17}$$

has a solution if and only if the Pick matrix

$$\mathcal{P}_{mn}[w] = \frac{1 - w_m w_n^*}{1 - z_m z_n^*}, \tag{2.18}$$

is positive semidefinite (PSD). The solution is unique if and only if the Pick matrix is singular.

Recall that a Hermitian matrix A is positive semidefinite if and only if $\mathbf{x}^\dagger A \mathbf{x} \geq 0 \ \forall \mathbf{x} \in \mathbb{C}^n$ [33]. By the spectral theorem, a Hermitian matrix has spectral decomposition $A = \sum_i \lambda_i \mathbf{c}_i \mathbf{c}_i^\dagger$ with $\lambda_i \in \mathbb{R}$ and the set $\{\mathbf{c}_i\}$ forms an orthonormal eigenbasis. It follows immediately that A is positive semidefinite if and only if all eigenvalues are nonnegative. If A has an eigenvector with negative eigenvalue $\lambda < 0$, then $\mathbf{v}^\dagger A \mathbf{v} = \lambda ||\mathbf{v}||^2 < 0$ and A is therefore not PSD.

To reformulate the Pick criterion in terms of the existence of a Nevanlinna interpolant, the Cayley transform [31, 34], $\mathscr{C} : \bar{\mathbb{C}}^+ \to \bar{\mathcal{D}}$, defined as

$$\mathscr{C}(z) = \frac{z - \mathrm{i}}{z + \mathrm{i}}, \tag{2.19}$$

is used as a one-to-one mapping between Nevanlinna and Schur functions. Note that the Cayley transform is applied to the function values and their domains. Substituting the Cayley transform into Eq. (2.18) yields a condition for the existence of a Nevanlinna interpolant. However, the corresponding Pick matrix can be simplified[7], and this simplification shows that the existence criterion may equivalently be expressed in terms of a significantly simpler matrix [29, 30, 35],

[6] Similarly, Matsubara data is henceforth understood to mean Matsubara Green's function data.

[7] There is also an issue of dimensional analysis when taking the Cayley transform of physical quantities.

Theorem 3 (The Nevanlinna–Pick criterion)**.** For a function $f \in \mathtt{N}$ to be determined, let $z_1, \ldots, z_N \in \mathbb{C}^+$ be distinct interpolation nodes, and let $f_1, \ldots, f_N \in \mathbb{C}^+$ be target values. The interpolation problem

$$f(z_m) = f_m, \quad m = 1, \ldots, N, \tag{2.20}$$

has a solution if and only if the Nevanlinna–Pick matrix

$$P_{mn}[f] = \frac{f_m - f_n^*}{z_m - z_n^*}, \tag{2.21}$$

is PSD. The solution is unique if and only if the Nevanlinna–Pick matrix is singular.

Formulated in terms of Matsubara data, the Nevanlinna–Pick matrix is[8]

$$P_{mn}[G] = \frac{i(G_m - G_n^*)}{\nu_m + \nu_n} \quad , \quad G_m = G(\mathbf{k}, \nu_m). \tag{2.22}$$

If the smallest eigenvalue of the Pick matrix in Eq. (2.22) is negative, the matrix is not PSD and therefore no Nevanlinna interpolant exists for the considered data. This means that any interpolant of the data must fail at least one of the defining Nevanlinna conditions: it is either not analytic in $\mathbb{C}^+$, does not have a positive imaginary part throughout $\mathbb{C}^+$, or both. In this way, the Pick criterion can be used to test if Matsubara data is compatible with a causal Green's function one $\mathbf{k}$-point at a time, without having to perform analytic continuation.

We emphasize that the Pick criterion for Matsubara data requires only a finite number of interpolation nodes. For an interpolation problem with infinitely many nodes [30], the failure of the Pick criterion for any matrix in the sequence $\{P_{n\times n}\}_{n=1}^{\infty}$ is sufficient to rule out the existence of a Nevanlinna interpolant for the infinite set of nodes. Thus, it is possible to prove that data on an infinite Matsubara grid is not causal, whereas proving causality on an infinite grid is less straightforward. In this work, we use failures of the Pick criterion to indicate violations of causality, rather than attempting to prove that Green's functions are causal.

By definition, the interpolation problem and the Pick matrix are specified in $\mathbb{C}^+$. The complex Green's function in $\mathbb{C}^-$ is obtained by imposing the symmetry relation

$$\mathscr{G}(\mathbf{k}, z^*) = [\mathscr{G}(\mathbf{k}, z)]^*, \tag{2.23}$$

which follows from Eq. (2.12). It should be noted that the Pick criterion can also be applied to other quantities, including self-energies and hybridization functions.

2.4 Systems

2.4.1 The Falicov–Kimball Model

The Falicov–Kimball model is one of the simplest models of interacting fermions [36, 37]. The model introduces two species of electrons: itinerant c electrons that can hop and localized

[8] Henceforth, the Nevanlinna–Pick matrix is simply referred to as the Pick matrix.

f electrons that cannot hop, depicted in Fig. 1. The spinless Falicov–Kimball model is a limiting case of the Hubbard model in which spin labels are mapped to species labels, $\uparrow \to f$ and $\downarrow \to c$, and the f electrons are taken to be immobile by setting their hopping parameter to zero [38]. The Hamiltonian is given by

$$\hat{H} = -t \sum_{\langle ij \rangle} \hat{c}_i^\dagger \hat{c}_j + U \sum_i \hat{n}_{c,i} \hat{n}_{f,i} - \mu \sum_i (\hat{n}_{c,i} + \hat{n}_{f,i}), \tag{2.24}$$

where $\hat{c}_i^\dagger, \hat{f}_i^\dagger$ are fermionic creation operators for a c- and f-electron at site i, respectively, and $\hat{c}_i$ and $\hat{f}_i$ are the corresponding annihilation operators. The nearest-neighbor hopping parameter is t, the on-site Coulomb repulsion between c and f electrons is U, μ denotes the chemical potential, and the particle number operators are defined as $\hat{n}_{c,i} = \hat{c}_i^\dagger \hat{c}_i$ and $\hat{n}_{f,i} = \hat{f}_i^\dagger \hat{f}_i$.

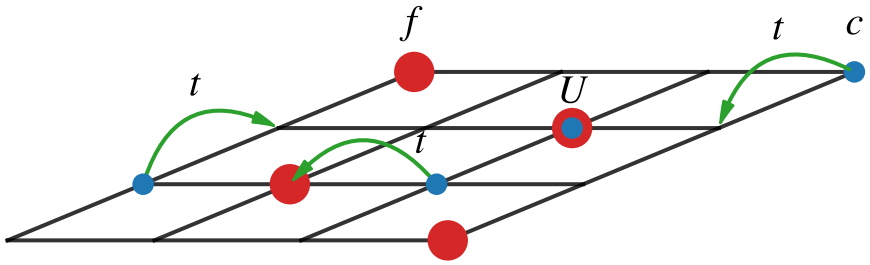

Figure 1: Illustration of the Falicov–Kimball model defined in Eq. (2.24). The itinerant c electrons are depicted as small blue dots, while localized f electrons are shown as larger red dots. Hopping of the c electrons lowers the energy, whereas simultaneous occupation of a site by a c and f electron increases the energy by the onsite Coulomb repulsion U.

The Falicov–Kimball model is semiclassical in the sense that the f-electron number operator at each site, $\hat{n}_{f,i}$, commutes with the Hamiltonian and can therefore be replaced by a binary variable, $\hat{n}_{f,i} \to n_{f,i}$, where $n_{f,i} = 1$ if site i is occupied by an f electron, and zero otherwise [39]. However, its thermal average is a continuous variable, $\langle \hat{n}_{f,i} \rangle \in [0, 1]$.

In addition, the itinerant c-electrons do not interact directly with one another, but only with the f-electrons through the Coulomb term in Eq. (2.24) [40]. Since the f-electrons are stationary, each fixed f-electron configuration acts as a static, configuration-dependent on-site potential for otherwise noninteracting c-electrons. Wick's theorem can therefore be applied for a fixed f-electron configuration, allowing two-particle quantities to be expressed in terms of single-particle quantities [12].

Since the Hamiltonian in Eq. (2.24) does not contain a hybridization term, the Green's function is diagonal,

$$G = \begin{pmatrix} -\langle \mathcal{T} \hat{c}_i(\tau) \hat{c}_j^\dagger \rangle & 0 \\ 0 & -\langle \mathcal{T} \hat{f}_i(\tau) \hat{f}_j^\dagger \rangle \end{pmatrix}. \tag{2.25}$$

The c-electron Green's function, $G_c(ij,\tau) = -\langle \mathcal{T}\hat{c}_i(\tau)\hat{c}_j^\dagger\rangle$, is typically the quantity of primary interest as it contains nontrivial dynamical information, unlike the f-electron Green's function since they are immobile and have flat dispersion bands. In this work, we therefore focus on the c-electron Green's function.

An important point in phase diagrams considered later is half filling, which is fixed by $\mu = \frac{U}{2}$. At this point, the thermal average of the occupation number is $\langle \hat{n}\rangle = 1/2$, meaning that a site is equally likely to be occupied or empty. The system is therefore particle-hole symmetric, a property with several further implications discussed elsewhere [41].

2.4.2 The Charge-Density Wave Phase

In two or higher dimensions, the half-filled Falicov–Kimball model undergoes a finite-temperature phase transition from a homogeneous disordered phase, in which the lattice sites are equivalent and no charge-density-wave order is present, to an ordered charge-density-wave (CDW) phase [42, 43]. In the CDW phase, the lattice decomposes into two inequivalent sublattices, A and B, characterized by different local electron densities,

$$\langle \hat{n}_f^A\rangle \neq \langle \hat{n}_f^B\rangle \quad , \quad \langle \hat{n}_c^A\rangle \neq \langle \hat{n}_c^B\rangle \,. \tag{2.26}$$

Specifically, the f-electron density becomes dominant on one sublattice, while the c-electron density becomes dominant on the other. As a result, the corresponding Green's functions and self-energies become sublattice dependent. The ordered phase therefore breaks discrete translational symmetry associated with a one-site lattice translation. Consequently, approximation schemes that assume translational invariance of the system, such as single-site DMFT, cannot be directly applied inside the CDW phase without modification [42].

The transition to the ordered phase is marked by a divergence of the static c-electron charge susceptibility accompanied by a corresponding divergence of the correlation length, indicating the onset of long-range order [42]. The CDW phase can also persist away from half filling, although doping generally suppresses the critical temperature [44]. The ordering vector $\mathbf{q}$ at which the susceptibility diverges indicates the spatial pattern of the CDW phase. In particular, if the susceptibility diverges at $\mathbf{q} = (\pi, \pi)$, the resulting CDW exhibits an alternating checkerboard pattern in the electron density.

Strictly speaking, true phase transitions occur only in the thermodynamic limit and are therefore absent in finite-size systems [45]. However, the approximation schemes considered in this work – the dual-fermion approximation and dynamical mean-field theory – do undergo a nonphysical phase transition even at finite system size [46]. Consequently, these methods should be regarded as less reliable in the vicinity of the predicted phase transitions.

2.4.3 The Anderson Insulating Phase

Electronic states may become strongly localized in the presence of disorder, a phenomenon known as Anderson localization. More specifically, disorder can inhibit the propagation of electronic wave functions, causing them to become spatially localized rather than extended throughout the system [47, 48]. Although the Falicov–Kimball model considered here contains no externally imposed disorder term, thermal averaging over f-electron configurations

can be viewed as generating an effective disorder potential for the c-electrons, which may induce Anderson localization at small values of U [49]. The Anderson insulating phase is characterized by a finite density of states at the Fermi energy. As the interaction strength U is increased, a gap appears in the density of states around the Fermi energy, and the insulating phase is instead identified as a Mott insulator [49, 50].

2.4.4 Impurity Models

The impurity problem considers an atom or molecule embedded in a metallic environment, called a bath, to which it couples by electron exchange [51]. The Anderson impurity model is a simple single-site impurity model [52]. Expressed in terms of the operators used in the Falicov–Kimball Hamiltonian, it can be written as [53]

$$\hat{H}_{\mathrm{imp}} = \underbrace{U\hat{n}_c n_f - \mu(n_f + \hat{n}_c)}_{\hat{H}_{\mathrm{loc}}} + \underbrace{\sum_{\mathbf{k}} \varepsilon(\mathbf{k}) \hat{d}^\dagger_{\mathbf{k}} \hat{d}_{\mathbf{k}}}_{\hat{H}_{\mathrm{bath}}} + \underbrace{\sum_{\mathbf{k}} (V_{\mathbf{k}} \hat{c}^\dagger \hat{d}_{\mathbf{k}} + V^*_{\mathbf{k}} \hat{d}^\dagger_{\mathbf{k}} \hat{c})}_{\hat{H}_{\mathrm{hyb}}} . \tag{2.27}$$

The isolated impurity is described by $\hat{H}_{\mathrm{loc}}$, while $\hat{H}_{\mathrm{bath}}$ describes the noninteracting metallic host, consisting of a band of itinerant electrons with dispersion $\varepsilon(\mathbf{k})$. Finally, $\hat{H}_{\mathrm{hyb}}$ describes the exchange of electrons between the impurity and the bath, with $V_{\mathbf{k}}$ denoting the hybridization matrix elements. The $\hat{d}_{\mathbf{k}}$ operators are associated with the bath while the $\hat{c}$ and $\hat{f}$ are the usual Falicov–Kimball operators acting on the impurity site. Note that only the c electrons couple to the bath since the f electrons cannot hop, and the impurity electrons do not interact directly with the bath electrons.

The thermal averages of observables can be expressed using the path integral formalism according to[9]

$$\langle O \rangle = \frac{\int \mathcal{D}[c^* c, d^* d, n_f] e^{-S} O[c^* c, d^* d, n_f]}{\int \mathcal{D}[c^* c, d^* d, n_f] e^{-S}}, \tag{2.28}$$

where c, c^* are Grassmann variables associated with the c impurity electrons, d, d^* are Grassmann variables associated with the bath electrons, and S is the action. If the operator O in Eq. (2.28) does not contain annihilation and creation operators associated with the bath, the integrals separate and the bath degrees of freedom can be integrated out [10]. As a result, one obtains an effective action, in which the effect of the bath on the impurity site is parametrized by the hybridization function $\Delta(\nu)$. For the considered impurity model, the effective action is[11] [44]

$$\begin{aligned} S_{\mathrm{eff}}[c, c^*, n_f] &= \sum_{\nu} (\Delta(\nu) - \mathrm{i}\nu - \mu + U n_f) c^*_\nu c_\nu - \beta \mu n_f, \\ &= -\sum_{\nu} (g_0^{-1}(\nu) - U n_f) c^*_\nu c_\nu - \beta \mu n_f, \end{aligned} \tag{2.29}$$

[9] The approximation schemes considered in this work are formulated within the action, or path integral, approach to quantum mechanics. We assume the reader is familiar with these concepts. For a more complete treatment, see [14, 54].

[10] See [14] for details.

[11] Here and throughout, we use the short-hand notation $c_\nu \equiv c(\nu)$ for Grassmann fields.

where $g_0(\nu)$ denotes the noninteracting impurity Green's function, and is given by [14]

$$g_0(\nu) = [\mathrm{i}\nu + \mu - \Delta(\nu)]^{-1}. \tag{2.30}$$

Once an effective action is specified by fixing the hybridization function, the partition function and Green's function can in principle be obtained from their path-integral representations [14, 54]. In practice, the path integrals are evaluated using techniques based on continuous-time quantum Monte Carlo [51], iterative perturbation theory [55], or other methods. However, for the single-site Falicov–Kimball impurity model, the interacting impurity Green's function can be obtained analytically as [56]

$$g(\nu) \equiv -\langle c_\nu c_\nu^* \rangle = (1 - \langle \hat{n}_f \rangle) g_0(\nu) + \langle \hat{n}_f \rangle \left[g_0^{-1}(\nu) - U \right]^{-1}. \tag{2.31}$$

2.5 Dynamical Mean-Field Theory

Dynamical mean-field theory (DMFT) [57] is a nonperturbative, causal [6, 7] approximation scheme for strongly correlated systems in which local effects dominate. It is used to construct an approximate Green's function by mapping the lattice system to a single-site impurity problem with fewer degrees of freedom. Solving this impurity problem yields the local impurity self-energy, which is then used as an approximation of the lattice self-energy. Consequently, the self-energy is purely local, meaning without momentum dependence, $\Sigma(\mathbf{k}, \nu) \approx \Sigma(\nu)$, since the impurity problem consists of a single site.

The mean-field aspect enters by treating a small set of degrees of freedom explicitly, in particular the impurity site, while incorporating the remaining degrees of freedom into an effective bath that acts on the impurity [58]. The mean field is parametrized by the noninteracting impurity Green's function, $g_0(\tau - \tau')$, from Eq. (2.30). Because this quantity depends on imaginary time, the theory is referred to as dynamical mean-field theory [57].

Similarly to other mean-field theories, DMFT is formulated in the thermodynamic limit, corresponding to an infinite lattice. In this limit, and more specifically in the limit of infinite coordination number (number of nearest neighbors), DMFT becomes exact. This is due to the suppression of nonlocal contributions to the self-energy: with the proper hopping scaling, these contributions vanish in the infinite-coordination limit, so that $\Sigma(\mathbf{k}, \omega) \to \Sigma(\omega)$. Since DMFT treats this local, frequency-dependent self-energy exactly through a self-consistent impurity problem, it becomes exact in the infinite-coordination limit [4].

The impurity-bath description is most natural for extended systems and is less directly applicable to small finite systems, where the picture of an impurity embedded in an effectively infinite environment becomes less appropriate. Consequently, applying single-site DMFT to a finite-size system introduces systematic errors, primarily due to the neglect of nonlocal correlations and finite-size effects. Nevertheless, DMFT remains a valuable starting point for studying strongly correlated systems of finite size [57, 59].

The hybridization function of the impurity problem is not known a priori, but is fixed by a self-consistency condition. Moreover, the self-consistency condition is used to update the hybridization function, i.e., the impurity bath, until the self-consistency condition is satisfied.

The conventional self-consistency equation within single-site DMFT is

$$G_{\mathrm{loc}}(\nu) \equiv \frac{1}{N}\sum_{\mathbf{k}} G_{\mathrm{DMFT}}(\mathbf{k},\nu) = g(\nu). \tag{2.32}$$

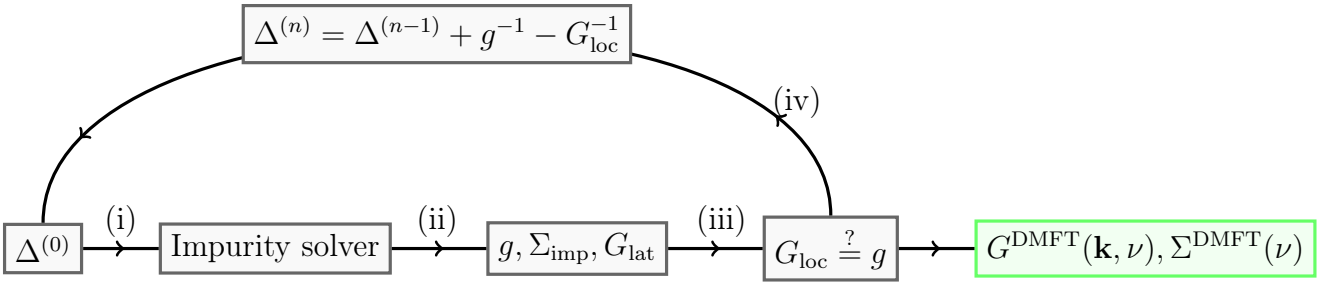

Figure 2: Schematic of the DMFT construction.

That is, the local projection of the lattice Green's function is identified with the impurity Green's function. The DMFT scheme is illustrated in Fig. 2, with corresponding steps [60]:

(i) An initial guess of the hybridization function, $\Delta^{(0)}(\nu)$ is used to define an effective impurity problem.

(ii) The impurity problem is solved, yielding the impurity self-energy. This self-energy is assigned to each lattice site, and the approximate lattice Green's function is constructed as

$$G_{\mathrm{lat}}(\mathbf{k},\nu) = \frac{1}{\mathrm{i}\nu - (\varepsilon(\mathbf{k}) - \mu) - \Sigma_{\mathrm{imp}}(\nu)}. \tag{2.33}$$

(iii) If the approximate lattice Green's function satisfies the self-consistency condition, the loop is terminated and the converged DMFT solution is obtained. Otherwise the hybridization function is updated according to

$$\Delta^{(\mathrm{new})}(\nu) = \Delta^{(\mathrm{old})}(\nu) + g^{-1}(\nu) - G_{\mathrm{loc}}^{-1}(\nu). \tag{2.34}$$

(iv) The new hybridization function updates the impurity bath and consequently defines a new impurity problem. The process is iterated until self-consistency is reached.

Note that from Eq. (2.34), the hybridization function is not updated when self-consistency is reached. Moreover, Eq. (2.34) can equivalently be expressed as

$$g_{0,\mathrm{new}}^{-1}(\nu) = \Sigma_{\mathrm{imp}} + G_{\mathrm{loc}}^{-1}(\nu). \tag{2.35}$$

2.5.1 Causality in Dynamical Mean-Field Theory

The DMFT scheme is known to be causal. Provided the initial hybridization function is causal, the Green's functions generated by the self-consistency loop satisfy $G_R(t<0)=0$, are analytic in $\mathbb{C}^+$, and have nonnegative spectral functions. In particular, if the impurity solver is causal, a causal hybridization function yields causal impurity Green's functions and self-energies. The nontrivial step is proving that the updated hybridization function generated from Eq. (2.35) remains causal [6, 7]. A proof of this can be found in Ref. [61].

For the DMFT implementation considered in this work, the initial hybridization function is taken as $\Delta^{(0)}(\nu)=\frac{t^2}{i\nu}$, where t is the hopping parameter. This hybridization function is causal[12].

2.6 The Dual-Fermion Approach

Single-site DMFT neglects nonlocal effects by assuming a momentum independent self-energy, which is not true for the exact solution. Various extensions of DMFT have been developed to incorporate nonlocal effects in different ways. In this work, we focus on the dual-fermion approach [5, 60, 62], which accounts for nonlocal effects through a diagrammatic expansion around the DMFT solution.

The dual-fermion approach is based on an exact change of variables from the original Grassmann fields of the physical electrons to a set of dual-fermion fields, $[c^*c]\to[\xi^*\xi]$. Self-consistency conditions are imposed such that the noninteracting dual-fermion system reproduces the DMFT Green's functions. Since the change of variables is exact, approximations enter only when specifying which diagrams to include in the dual interaction potential.

2.6.1 Derivation of Dual Transformation

The formal derivation of the transformation to the dual fields is readily available in the literature [5, 62, 63]; here, we simply sketch the essential steps.[13] The change of variables is based on expressing the action in terms of local impurity actions defined at each lattice site i,

$$S[c^*c,n_f]=\sum_i S_{\mathrm{imp}}[c_i^*c_i,n_f]-\sum_{\nu\mathbf{k}}(\Delta_\nu-\varepsilon_{\mathbf{k}})c^*_{\mathbf{k}\nu}c_{\mathbf{k}\nu}, \tag{2.36}$$

$$S_{\mathrm{imp}}[c_i^*c_i,n_f]=\sum_\nu(\Delta_\nu-\mathrm{i}\nu-\mu+Un_f)c^*_{i\nu}c_{i\nu}-\beta\mu n_f. \tag{2.37}$$

Here, c and ξ without indices denote the sets of Grassmann fields associated with the lattice fermions and the dual fermions, respectively. The dual fermionic fields are introduced by the Hubbard–Stratonovich transformation [54],

$$e^{Ac^*c}=\frac{A}{\alpha^2}\int d\xi^*d\xi\; e^{-A^{-1}\alpha^2\xi^*\xi-\alpha(c^*\xi+\xi^*c)}, \tag{2.38}$$

[12] This follows from the Fourier representation of the Heaviside function [3], as $\Theta(t)=-\frac{1}{2\pi i}\int d\omega\;\frac{e^{-i\omega t}}{\omega+i\eta}=-\frac{1}{it^2}\Delta_{0,R}(t)$, since $\Delta_{0,R}(\omega)=t^2[\omega+i\eta]^{-1}$. Moreover, $-\mathrm{Im}\Delta_0(z)=t^2\frac{\mathrm{Im}z}{|z|^2}>0$ for $z\in\mathbb{C}^+$.

[13] To simplify notation, the arguments of relevant quantities are written as indices in this section.

applied to each set of indices $\mathbf{k}\nu$, with $A_{\mathbf{k}\nu} = (\Delta_\nu - \varepsilon_{\mathbf{k}})$, and $\alpha_\nu = g_\nu^{-1}$ being the impurity Green's function. The transformation is completed by integrating out the original lattice fermions. This is done by performing the integrals over the original lattice degrees of freedom independently and noting that they yield impurity expectation values involving the dual fields,

$$Z = \int \mathcal{D}[\xi^*\xi] e^{-S_{\mathrm{DF}}[\xi^*\xi]} \prod_i Z_{i,\mathrm{imp}} \left\langle e^{-\sum_\nu g_\nu^{-1}(c_{i\nu}^* \xi_{i\nu} + \xi_{i\nu}^* c_{i\nu})} \right\rangle_{\mathrm{imp}}. \tag{2.39}$$

Here, $Z_{i,\mathrm{imp}}$ are the impurity partition functions of the original lattice fermions, and $S_{\mathrm{DF}}[\xi^*\xi]$ is the part of the action containing only ξ, ξ^* fields. To obtain the action in terms of dual fields only, the cumulant expansion [20, 64] is used to rewrite the expectation value of an exponential as an exponential of its cumulant series[14]. The dual action is then obtained as

$$S[\xi^*\xi] = -\sum_{\mathbf{k}\nu} \tilde{G}_0(\mathbf{k},\nu) \xi_{\mathbf{k}\nu}^* \xi_{\mathbf{k}\nu} + \sum_i V[\xi_i^*\xi_i], \tag{2.40}$$

where the interaction potential is determined by evaluating the cumulants of the impurity expectation values in Eq. (2.39). Moreover, the bare dual Green's function is obtained as

$$\tilde{G}_0(\mathbf{k},\nu) = [g(\nu)^{-1} + \Delta(\nu) - \varepsilon(\mathbf{k})]^{-1} - g(\nu) = G_{\mathrm{lat}}(\mathbf{k},\nu) - g(\nu), \tag{2.41}$$

where $G_{\mathrm{lat}}(\mathbf{k},\nu)$ is the lattice Green's function generated from the impurity problem, not necessarily the converged DMFT solution.

As mentioned, the transformation to dual degrees of freedom is exact, meaning that the dual-fermion approach would generate exact results provided that the perturbative expansion converges and that all contributing diagrams are included. The leading term in the dual interaction potential is[15] [63, 65]

$$\begin{aligned} V^{(2)}[\xi_i^*\xi_i] &= -\frac{1}{4} \sum_i \sum_{\nu\nu'\Omega} \gamma_{\nu\nu'\Omega} \xi_{\nu i}^* \xi_{\nu+\Omega i} \xi_{\nu'+\Omega i}^* \xi_{\nu' i}, \\ &= -\frac{1}{4N} \sum_{\mathbf{k}\mathbf{k}'\mathbf{q}} \sum_{\nu\nu'\Omega} \gamma_{\nu\nu'\Omega} \xi_{\nu\mathbf{k}}^* \xi_{\nu+\Omega,\mathbf{k}+\mathbf{q}} \xi_{\nu'+\Omega,\mathbf{k}'+\mathbf{q}}^* \xi_{\nu'\mathbf{k}'}. \end{aligned} \tag{2.42}$$

Here, $\gamma(\nu,\nu',\Omega)$ is the two-particle impurity vertex function, defined by the perturbative expansion of the interaction potential. Since it is obtained in the second order expansion of Eq. (2.39), it depends on the two-particle impurity Green's function $g^{(2)}(\nu,\nu',\Omega) = \langle c_\nu c_{\nu+\Omega}^* c_{\nu'+\Omega} c_{\nu'}^* \rangle$, where Ω is a bosonic Matsubara frequency [66], which is a difference of two fermionic Matsubara frequencies. The diagrammatic representation[16] of the interaction term in Eq. (2.42) is shown in Fig. 3.

[14] The cumulant expansion is given by $\langle e^{c\hat{A}} \rangle = \exp\left(\sum_{n=1}^{\infty} \frac{c^n}{n!} \kappa_n\right)$, where κ_n is the nth cumulant of $\hat{A}$, given in Ref. [20].

[15] Note that the dual interaction potential $V[\xi_i^*\xi_i]$ is local in real space, but nonlocal in Matsubara-frequency and momentum space.

[16] For the diagrammatic rules of the dual-fermion formalism, see Refs. [41, 67].

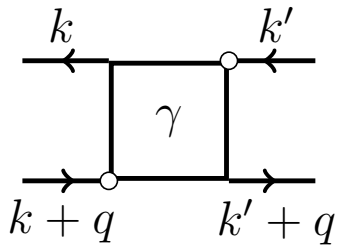

Figure 3: Diagrammatic representation of the two-particle interaction term in Eq. (2.42), where $k = (\mathbf{k}, \nu), k' = (\mathbf{k}', \nu')$ and $q = (\mathbf{q}, \Omega)$ denote combined momentum and Matsubara-frequency labels. Incoming lines with labels $k + q$ and k' scatter into outgoing lines with labels k and $k' + q$.

As discussed in Sec. 2.4.1, the Falicov–Kimball impurity model can be written as the weighted average over two impurity configurations, corresponding to the absence or presence of an f-electron. For each fixed configuration, the problem corresponds to noninteracting c-electrons, meaning Wick's theorem can be applied, allowing two-particle quantities to be expressed in terms of single-particle quantities [12]. Consequently, the impurity vertex function can be obtained from single-particle Green's functions according to [12, 44]

$$\gamma(\Omega, \nu, \nu') = w_1 w_0 U^2 (\delta_{\Omega,0} - \delta_{\nu,\nu'}) \Lambda_\nu \Lambda_{\nu'+\Omega} \quad , \quad \Lambda_\nu = g_0^{-1}(\nu)[g_0^{-1}(\nu) - U]^{-1} g^{-2}(\nu), \tag{2.43}$$

where $w_1 = \langle \hat{n}_f \rangle$ and $w_0 = 1 - \langle \hat{n}_f \rangle$. The delta functions in Eq. (2.43) reduce the frequency dependence of the impurity vertex function to two independent frequencies. In the static limit ($\Omega = 0$), the factor $(1 - \delta_{\nu\nu'})$ reflects the Pauli principle. For dynamic scattering ($\Omega \neq 0$), the impurity vertex is diagonal in fermionic Matsubara frequencies.

2.6.2 Dual Relations and Self-Energy

The lattice and dual Green's functions are related through

$$G(\mathbf{k}, \nu) = [\Delta(\nu) - \varepsilon_{\mathbf{k}}]^{-1} + g^{-2}(\nu)[\Delta(\nu) - \varepsilon_{\mathbf{k}}]^{-2} \tilde{G}(\mathbf{k}, \nu), \tag{2.44}$$

where $\tilde{G}(\mathbf{k}, \nu) = -\langle \xi_{\mathbf{k}\nu} \xi^*_{\mathbf{k}\nu} \rangle$ and $G(\mathbf{k}, \nu) = -\langle c_{\mathbf{k}\nu} c^*_{\mathbf{k}\nu} \rangle$ [5]. The bare and interacting dual Green's functions are related by the Dyson equation, which defines the dual self-energy,

$$\tilde{\Sigma}(\mathbf{k}, \nu) = \tilde{G}_0^{-1}(\mathbf{k}, \nu) - \tilde{G}^{-1}(\mathbf{k}, \nu). \tag{2.45}$$

Moreover, Eq. (2.44) can be used to obtain the following expression of lattice self-energy in terms of the dual and impurity self-energies [63, 68],

$$\Sigma(\mathbf{k}, \nu) = \Sigma_{\text{imp}}(\nu) + \frac{\tilde{\Sigma}(\mathbf{k}, \nu)}{1 + \tilde{\Sigma}(\mathbf{k}, \nu) g(\nu)}. \tag{2.46}$$

2.6.3 The Ladder Approximation

In the particle-hole symmetric Falicov–Kimball model, $\mu = U/2$, impurity vertex functions of order higher than two vanish. Consequently, Eq. (2.42) gives the full interaction term [44]. Away from particle-hole symmetry, we approximate the dual interaction potential by retaining only the two-particle impurity vertex. Within this approximation, we further restrict the diagrammatic contributions to ladder diagrams in the electron-hole channel, which describe repeated particle-hole scattering. The ladder diagrams incorporate long-range fluctuations and capture collective behavior associated with the CDW phase. However, critical temperatures signaling the onset of order are generally suppressed by the ladder diagrams [65, 69]. The ladder-renormalized vertex function, Γ, is obtained from the Bethe-Salpeter equation (BSE). The dual Bethe-Salpeter equation is [44, 60, 66]

$$\tilde{\Gamma}_{\mathbf{q}\nu\nu'\Omega} = \gamma_{\nu\nu'\Omega} + \sum_{\nu''} \gamma_{\nu\nu''\Omega} \tilde{\chi}^{(0)}_{\mathbf{q}\nu''\Omega}(\mathbf{q}) \tilde{\Gamma}_{\mathbf{q}\nu''\nu'\Omega} \quad , \quad \tilde{\chi}^{(0)}_{\mathbf{q}\nu\Omega} = -\frac{T}{N} \sum_{\mathbf{k}} \tilde{G}_{\mathbf{k}\nu} \tilde{G}_{\mathbf{k}+\mathbf{q}\nu+\Omega}, \tag{2.47}$$

where $\tilde{\chi}^{(0)}_{\mathbf{q}\nu\Omega}$ is the bare dual-fermion bubble. Note that, unlike the impurity vertex function, the renormalized dual vertex function is nonlocal in transfer momentum due to the fermionic bubble. The diagrammatic representation of the Bethe-Salpeter equation is shown in Fig. 4 [66, 70].

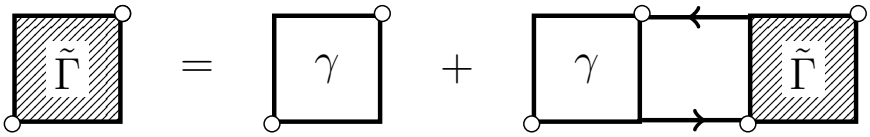

Figure 4: Diagrammatic representation of the Bethe-Salpeter equation in the electron-hole channel. Arrows represent interacting dual Green's functions.

The Bethe-Salpeter equation is solved independently at each $(\mathbf{q}, \Omega)$-point by writing Eq. (2.47) as a matrix equation in fermionic Matsubara frequencies,

$$\tilde{\Gamma}_{\mathbf{q}\Omega} = [1 - \gamma_\Omega \mathrm{diag}(\tilde{\chi}^{(0)}_{\mathbf{q}\Omega})]^{-1} \gamma_\Omega. \tag{2.48}$$

Hence, for the dual vertex to converge, all eigenvalues of the matrix $\gamma_\Omega \mathrm{diag}(\tilde{\chi}^{(0)}_{\mathbf{q}\Omega})$ must satisfy $|\lambda| < 1$.

Formally, the dual self-energy is obtained by summing all topologically distinct diagrams with one incoming and one outgoing external fermion line, provided the diagrams cannot be split into separate pieces by cutting dual Green's function lines [41]. For the ladder diagrams considered here, the corresponding diagrammatic representation of the self-energy is depicted in Fig. 5, and the associated algebraic expression is [44, 63]

$$\tilde{\Sigma}(\mathbf{k}, \nu) = \sum_{\mathbf{q},\Omega} \tilde{\Gamma}(\mathbf{q}, \nu, \nu, \Omega) \tilde{G}(\mathbf{k} + \mathbf{q}, \nu + \Omega), \tag{2.49}$$

from which the lattice self-energy is obtained using Eq. (2.46).

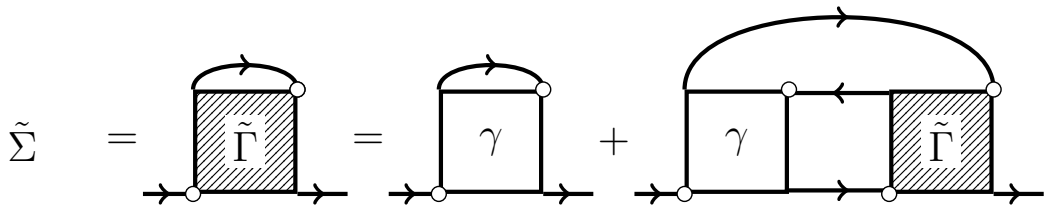

Figure 5: Diagrammatic expression of the dual self-energy $\tilde{\Sigma}$ in the ladder approximation.

2.6.4 Static and Dynamic Scattering

The bosonic Matsubara frequency label in the BSE is an external label. Consequently, the renormalized vertex $\tilde{\Gamma}$ can be written as the sum of a static sector, $\Omega = 0$, and a dynamic sector, $\Omega \neq 0$ [12]. The corresponding contributions to the dual self-energy can therefore be evaluated separately in Eq. (2.49).

$$\tilde{\Sigma}(\mathbf{k}, \nu) = \tilde{\Sigma}^{\text{static}}(\mathbf{k}, \nu) + \tilde{\Sigma}^{\text{dynamic}}(\mathbf{k}, \nu). \tag{2.50}$$

In the static sector, the BSE remains a matrix equation in the fermionic Matsubara frequencies. In the dynamic sector, however, the special frequency structure of the Falicov–Kimball impurity vertex, Eq. (2.43), makes the BSE diagonal in fermionic frequency. As such, the dual vertex is obtained from independent scalar equations for dynamic scattering.

The static channel, $\Omega = 0$, is of particular interest, since a divergence of the static c-electron charge susceptibility signals the onset of the CDW ordered phase. In the Falicov–Kimball model, the static and dynamic susceptibilities decouple. Consequently, the dynamical charge susceptibility does not in general signal the onset of the CDW phase [13]. In the static channel, the renormalized dual vertex function can be expressed analytically as [44]

$$\tilde{\Gamma}(\mathbf{q}, \nu, \nu') = \phi(\mathbf{q}, \nu) \frac{\Lambda(\nu') - \Lambda(\nu)\delta_{\nu\nu'} + B(\mathbf{q}, T)\Lambda(\nu)\delta_{\nu\nu'} - \phi(\mathbf{q}, \nu')\Lambda^2(\nu')\tilde{\chi}^0(\mathbf{q}, \nu')}{1 - B(\mathbf{q}, T)}, \tag{2.51}$$

$$\phi(\mathbf{q}, \nu) = \frac{w_1 w_0 U^2 \Lambda(\nu)}{1 + w_1 w_0 U^2 \Lambda^2(\nu)\tilde{\chi}^0(\mathbf{q}, \nu)} \quad , \quad B(\mathbf{q}, T) = \sum_{\nu} \phi(\mathbf{q}, \nu)\Lambda(\nu)\tilde{\chi}^0(\mathbf{q}, \nu), \tag{2.52}$$

with $\Lambda(\nu)$ defined in Eq. (2.43) and $w_1 = \langle \hat{n}_f \rangle$, $w_0 = 1 - \langle \hat{n}_f \rangle$.

2.6.5 Computational Scheme

Similarly to DMFT, the hybridization function is not known a priori within the dual-fermion approach, but is fixed by the self-consistency condition and is subsequently obtained through an iterative process.

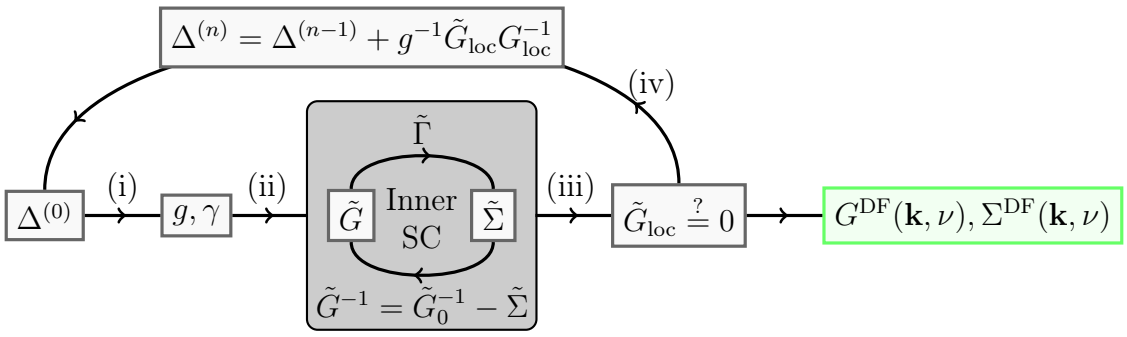

Figure 6: Illustration of the dual-fermion computational scheme.

The dual-fermion computational scheme is illustrated in Fig. 6 and proceeds as follows [5, 44, 60, 63]:

(i) An initial guess for the hybridization function, $\Delta^{(0)}$, is used to define an effective impurity problem; in practice, the converged DMFT hybridization is often used. The impurity problem is then solved to obtain the impurity Green's function, $g(\nu)$, and the impurity vertex function, $\gamma(\nu, \nu', \Omega)$. For the Falicov–Kimball model, the impurity solver consists of the analytical expressions given in Sec. 2.4.1.

(ii) The inner dual-fermion loop is initialized by computing the bare dual Green's function, $\tilde{G}_0(\mathbf{k}, \nu)$, and the renormalized dual vertex function, $\tilde{\Gamma}(\mathbf{q}, \nu, \nu', \Omega)$. Initially, the dual self-energy is set to zero $\tilde{\Sigma}(\mathbf{k}, \nu) \equiv 0$, such that $\tilde{G} = \tilde{G}_0$. The self-energy is then computed from the dual Green's function, and the dual vertex according to Eq. (2.49). The dual Green's function is subsequently updated using the Dyson equation, $\tilde{G}^{-1} = \tilde{G}_0^{-1} - \tilde{\Sigma}$. The process is repeated until the dual Green's function has converged, or until a set maximum number of iterations is reached.

(iii) After termination of the inner loop, the dual Green's function is checked against the imposed self-consistency condition. In Fig. 6, $\tilde{G}_{\rm loc}(\nu) = 0$ is shown as an example of such a condition.[17] If the condition is satisfied, the calculation is terminated, and the lattice Green's function and self-energy are obtained by the dual transformation equations in Sec. 2.6.2.

(iv) If the self-consistency condition is not satisfied, the hybridization is updated and the entire procedure is repeated until convergence is reached.

Note that the hybridization update reflects the self-consistency condition; at convergence, $\Delta^{(n)} = \Delta^{(n-1)}$. In practice, mixing is often introduced to improve convergence and avoid oscillatory behavior around the converged value [5],

$$\Delta^{(n)}_{\rm mixed} = \alpha\Delta^{(n)} + (1-\alpha)\Delta^{(n-1)} \quad , \quad \tilde{G}^{(n)}_{\rm mixed} = \alpha\tilde{G}^{(n)} + (1-\alpha)\tilde{G}^{(n-1)}. \tag{2.53}$$

[17] Self-consistency conditions are discussed in detail in the next section.

For the hybridization function, this is equivalent to performing the update $\Delta^{(n)} = \Delta^{(n-1)} + \alpha[g^{-1}\tilde{G}_{\mathrm{loc}}G_{\mathrm{loc}}^{-1}]$. This mixing procedure does not by itself guarantee convergence. In practice, convergence can remain challenging, particularly close to the CDW phase boundary, even when mixing is used.

2.6.6 Self-Consistency Conditions

Dual-fermion self-consistency conditions should be constructed such that the DMFT self-consistency condition is obtained in the absence of dual interactions, $\tilde{\Sigma}(\mathbf{k}, \nu) = 0$. Examples of such self-consistency conditions are [5, 60, 63]

$$\text{(i)} \ \sum_{\mathbf{k}} \tilde{G}(\mathbf{k}, \nu) = 0 \quad , \quad \text{(ii)} \ g(\nu) = \frac{1}{N} \sum_{\mathbf{k}} G(\mathbf{k}, \nu) \quad , \quad \text{(iii)} \ \sum_{\mathbf{k}} \tilde{G}_0(\mathbf{k}, \nu) = 0, \tag{2.54}$$

where $G(\mathbf{k}, \nu)$ is the Green's function obtained from the converged inner dual-fermion loop, and $\tilde{G}(\mathbf{k}, \nu)$ is the corresponding dual Green's function. Note that condition (iii) is equivalent to the DMFT self-consistency condition by Eq. (2.41). When interactions are included, the self-consistency conditions in Eq. (2.54) are no longer equivalent to the DMFT condition and generally lead to hybridization functions that differ from the DMFT hybridization function.

A particularly convenient choice is the self-consistency condition (i), which forces all diagrammatic contributions that contain simple closed loops to vanish [5]. In particular, the self-energy contribution in Fig. 5 containing a single γ-vertex is zero. In this work, we restrict attention to this self-consistency condition, with the hybridization function updated as described in the previous section.

2.6.7 Causality in the Dual-Fermion Approach

In the literature, it has been argued that the dual-fermion approach preserves causality, in the sense that the resulting retarded Green's functions satisfy $G_R(t < 0) = 0$, provided that the hybridization function used to initialize the self-consistency loop is itself causal. However, a formal proof of this claim, or that the corresponding spectral function remains strictly positive has not yet been established [5]. This issue is not strictly formal, as when nonlocal correlation effects are included in the self-consistency cycle, the conventional DMFT self-consistency condition, $\frac{1}{N}\sum_{\mathbf{k}} G(\mathbf{k}, \nu) = g(\nu)$, need not produce strictly positive spectral functions [21]. As discussed in Sec. 2.5.1 and in Ref. [21], noncausality (in the sense of negative spectral functions) can arise from the self-consistency condition relations, particularly when nonlocal effects are included.

Another key aspect of causality in the dual-fermion approach is the choice of diagrams included in the perturbative expansion. In standard diagrammatic perturbation theory, a set of rules exists to ensure that a given diagrammatic approximation produces nonnegative spectral functions [8]. The idea of these rules is to factorize the self-energy into half-diagrams, which are then combined with their complex conjugates to form Hermitian products, thereby guaranteeing nonnegative spectral functions. In a similar spirit, perturbative expansions around DMFT are not guaranteed to be causal for arbitrary choices of diagrams. Expanding

around a causal self-energy is intrinsically delicate, since the corrections must be sufficiently constrained to redistribute spectral weight without violating nonnegativity. The diagrammatic choices made in ladder dual-fermion theory, and their implications for causality, are therefore of central interest in this work.

3 Method

To compute the DMFT and DF Green's functions for the Falicov–Kimball model, we use the open-source implementation developed by A. Antipov [44, 70]. The impurity solver in this implementation consists of the analytic formulas discussed in Sec. 2.5, and the dual-fermion Green's functions are computed within the ladder approximation described in Sec. 2.6.3. The exact Green's functions are computed for small systems using the implementation developed by A. Mishra. A description of the calculation procedure can be found in Ref. [46]. The idea is to construct the Green's function for each fixed f-electron configuration and then average the resulting configuration-dependent Green's functions using the corresponding thermal weights.

The dual-fermion Green's function is calculated using only the static contribution to the BSE, as the latest version of A. Antipov's implementation supports only this channel. Throughout this work, we consider only two-dimensional systems with periodic boundary conditions, and denote the side length by L.

3.1 Computational Schemes and Default Parameters

As discussed in Sec. 2.6.7, causality violations may arise either from the choice of diagrams or from updates to the hybridization function during the self-consistency cycle. Moreover, several layers of self-consistency may introduce numerical artifacts, leading to noncausal Green's functions. To probe these possible sources of causality violations, we consider two sets of default parameters for the dual-fermion computations.

(i) One-shot Dual Fermion: The converged DMFT hybridization function initializes the dual-fermion loop, in which a single inner-loop iteration is performed to update the hard-coded initial dual self-energy, $\tilde{\Sigma}^{(0)} = 0$, once. Both the inner and outer loops are then terminated, and the updated dual self-energy $\tilde{\Sigma}^{(1)}$ is used to construct the lattice Green's function. The parameters used for the one-shot computations are given in Table 1.[18]

$N_{\mathrm{DF,Outer}}$	$N_{\mathrm{DF,Inner}}$	$\alpha_{\mathrm{DF,Inner}}$
1	1	1

Table 1: Default simulation parameters for the one-shot DF computations. The maximum number of outer- and inner-loop iterations are denoted by $N_{\mathrm{DF,Outer}}$ and $N_{\mathrm{DF,Inner}}$, respectively. The mixing parameter used in the inner loop is $\alpha_{\mathrm{DF,Inner}}$, where unity corresponds to no mixing with the dual Green's function from the previous iteration.

[18] Note that $N_{\mathrm{DF,Outer}} = 0$ corresponds to the DMFT solution, as the dual-fermion loop is never initialized.

(ii) Self-consistent Dual Fermion: The converged DMFT hybridization function initializes the dual-fermion loop, in which several layers of inner and outer self-consistency iterations are performed until a specified convergence criterion is satisfied within a given tolerance, or until the maximum number of iterations is reached. The convergence criteria are:

$$\begin{aligned} &\text{Outer-loop convergence condition :} && \tfrac{1}{N_\nu}\textstyle\sum_\nu |\Delta^{(n)}(\nu) - \Delta^{(n-1)}(\nu)| \leq \varepsilon_{\mathrm{DF,Outer}}, \\ &\text{Inner-loop convergence condition :} && \tfrac{1}{N_{\mathbf{k}}N_\nu}\textstyle\sum_{\mathbf{k},\nu} |\tilde{G}^{(n)}(\mathbf{k},\nu) - \tilde{G}^{(n-1)}(\mathbf{k},\nu)| \leq \varepsilon_{\mathrm{DF,Inner}}. \end{aligned} \tag{3.1}$$

The parameters used for the self-consistent dual-fermion computations are given in Table 2.

$N_{\mathrm{DF,Outer}}$	$\varepsilon_{\mathrm{DF,Outer}}$	$N_{\mathrm{DF,Inner}}$	$\varepsilon_{\mathrm{DF,Inner}}$	$\alpha_{\mathrm{DF,Inner}}$	$\alpha_{\mathrm{DF,Outer}}$
30	10^{-7}	50	10^{-7}	0.8	0.8

Table 2: Default simulation parameters for the self-consistent DF calculations. Mixing is used in both loops to improve convergence and avoid oscillatory behavior.

It is important to avoid setting the maximum number of iterations too high, since the implementation tends to get stuck near the CDW boundary. For the scans considered in the results, the parameters in Table 2 always led to convergence outside of the CDW phase.

N_{DMFT}	N_ν	t
1000	96	1

Table 3: Default simulation parameters used for all DF simulations. The DMFT loop is terminated when a convergence criterion analogous to the outer-loop criterion in Eq. (3.1) is satisfied up to the hard-coded tolerance $\varepsilon_{\mathrm{DMFT}} = 10^{-8}$, or when the number of iterations exceeds N_{DMFT}. The number of positive Matsubara frequencies used is denoted by N_ν, and t denotes the hopping parameter.

Note that the mixing parameter $\alpha_{\mathrm{DF,Outer}}$ updates the hybridization function both during the initial DMFT loop and later in the outer DF loop. Since the mixing does not affect the converged value, the same DMFT hybridization function will initialize both the one-shot and self-consistent calculations, provided that enough iterations are used to ensure proper convergence. Default parameters used in both approaches are given in Table 3.

The hopping parameter is fixed to unity throughout, and effects of changing the number of Matsubara frequencies are discussed in the results.

3.2 Numerical Aspects of the CDW Phase

The condition $B(\mathbf{q}, T) = 1$ marks the onset of the CDW phase, where the dual vertex $\tilde{\Gamma}$, and hence the static c-electron charge susceptibility, diverges [44]. The ordered phase corresponds to $B(\mathbf{q}, T) \geq 1$. Since the approximation schemes considered are not applicable inside this

phase, we restrict our calculations to the disordered side. Near the phase boundary, however, dual-fermion corrections are expected to become significant due to the growing importance of nonlocal effects near the onset of long-range order [69]. We stress again that the phase transition is an artifact of applying approximation schemes formulated in the thermodynamic limit, and would not appear in the exact solution for finite-size lattices. The CDW regions for the computational approaches considered are shown in Fig. 7.

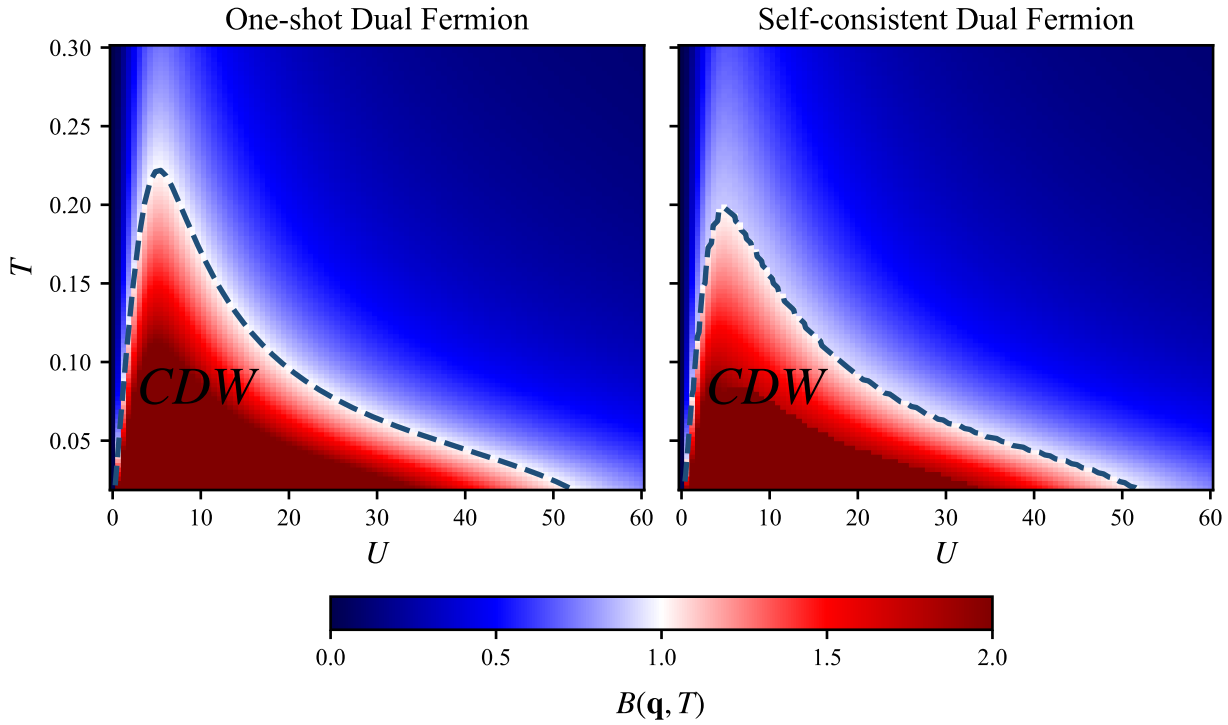

Figure 7: Parameter-space diagram of $B(\mathbf{q}, T)$ evaluated at $\mathbf{q} = (\pi, \pi)$ at half filling for a $L = 4$ system. The dotted line indicates $B(\mathbf{q}, T) = 1$, with the CDW regime lying below it. For the $L = 4$ system, CDW instabilities at other ordering vectors are contained within the dome formed by the $\mathbf{q} = (\pi, \pi)$ instability and therefore do not give rise to additional instability regions or further regions that should be excluded from the analysis.

The quantity $B(\mathbf{q}, T)$ provides a measure of distance to the CDW phase. Close to the phase boundary, numerical instabilities arise as $[1 - B(\mathbf{q}, T)]^{-1}$ approaches a singularity. Therefore, apparent deviations from causality near the phase boundary must be checked carefully to distinguish genuine causality violations from numerical artifacts.

3.3 Verification of Positive Semidefiniteness

The smallest Pick eigenvalue is used to investigate causality violations. If this eigenvalue is negative and its magnitude exceeds a set tolerance, the Pick matrix is interpreted as not being PSD. To determine whether this corresponds to a causality violation, additional physical factors, such as the distance from the CDW boundary, must be considered.

The smallest eigenvalues of Pick matrices are highly sensitive to finite-precision errors due to their large spectral condition numbers, $\kappa(P) = \frac{|\lambda_{\max}|}{|\lambda_{\min}|}$ [35]. Moreover, in floating-point numerical calculations, computed eigenvalues are generally accurate only up to a scale proportional to $\varepsilon_{\text{machine}}||A||_2$ [71]. In this work, we use the tolerance

$$|\lambda_{\text{num}} - \lambda_{\text{exact}}| = \delta\lambda \leq Cn\varepsilon_{\text{machine}}||A||_2, \tag{3.2}$$

where $C > 0$ is a constant, n is the matrix dimension, $\varepsilon_{\text{machine}}$ denotes the machine precision, and $||A||_2$ is the 2-norm of matrix A. For Hermitian matrices, this norm is given by $||A||_2 = \max_i |\lambda_i(A)|$. For a $L = 4$ system with 96 positive Matsubara frequencies and $C = 100$, the largest error estimate obtained from Eq. (3.2) was approximately $\delta\lambda \approx 10^{-10}$ when scanning over T and U at half filling. This value is therefore used as the eigenvalue tolerance.[19]

4 Results

4.1 Benchmarking Approximation Schemes – 4×4 Systems

In sufficiently small systems, the exact Green's function can be computed and used as a reference for benchmarking approximation schemes, despite the greater computational cost. In this section, we assess the accuracy of the approximation schemes for a $L = 4$ system by comparing them against the exact results. The benchmarks are performed away from the CDW phase at the inequivalent lattice momenta $\boldsymbol{\Gamma} = (0, 0)$, $\boldsymbol{Y}' = \left(0, \frac{\pi}{2}\right)$ and $\boldsymbol{M}' = \left(\frac{\pi}{2}, \frac{\pi}{2}\right)$.

In comparing the results, it is important to distinguish how CDW correlation effects enter the different approaches. In DMFT, the Green's function is obtained directly from the single-site impurity self-energy, while the BSE can be solved separately to compute the susceptibility and investigate the CDW instability. Thus, CDW-related nonlocal correlations do not feed back into the single-particle Green's function during its construction in DMFT. In contrast, in DF computations, the self-energy is constructed directly from the renormalized dual vertex function. Consequently, CDW-related effects enter the dual Green's function through construction of the dual self-energy.

4.1.1 Comparison with Exact Diagonalization at Half Filling

To quantify the accuracy of the approximation schemes, we introduce the deviation from the exact solution, $\delta G_{\text{ED}}(\mathbf{k}, \nu) = G_{\text{ED}}(\mathbf{k}, \nu) - G_{\text{approx}}(\mathbf{k}, \nu)$, and the norm

$$||\delta G(\mathbf{k})|| = \sqrt{\frac{1}{2N_\nu} \sum_{n=-N_\nu}^{N_\nu - 1} |\delta G(\mathbf{k}, \nu_n)|^2} = \sqrt{\frac{1}{N_\nu} \sum_{n=0}^{N_\nu - 1} |\delta G(\mathbf{k}, \nu_n)|^2}, \tag{4.1}$$

[19] We also considered inspecting the eigenvector associated with the smallest Pick eigenvalue. A structured eigenvector may indicate separation from the near-zero noise subspace, but the sign and magnitude of its eigenvalue remain unreliable below the chosen tolerance. Hence, this test alone does not provide a conclusive test for a genuinely negative eigenvalue.

where the equality follows from Eq. (2.23) and assuming a similar relation holds for the approximate solution.

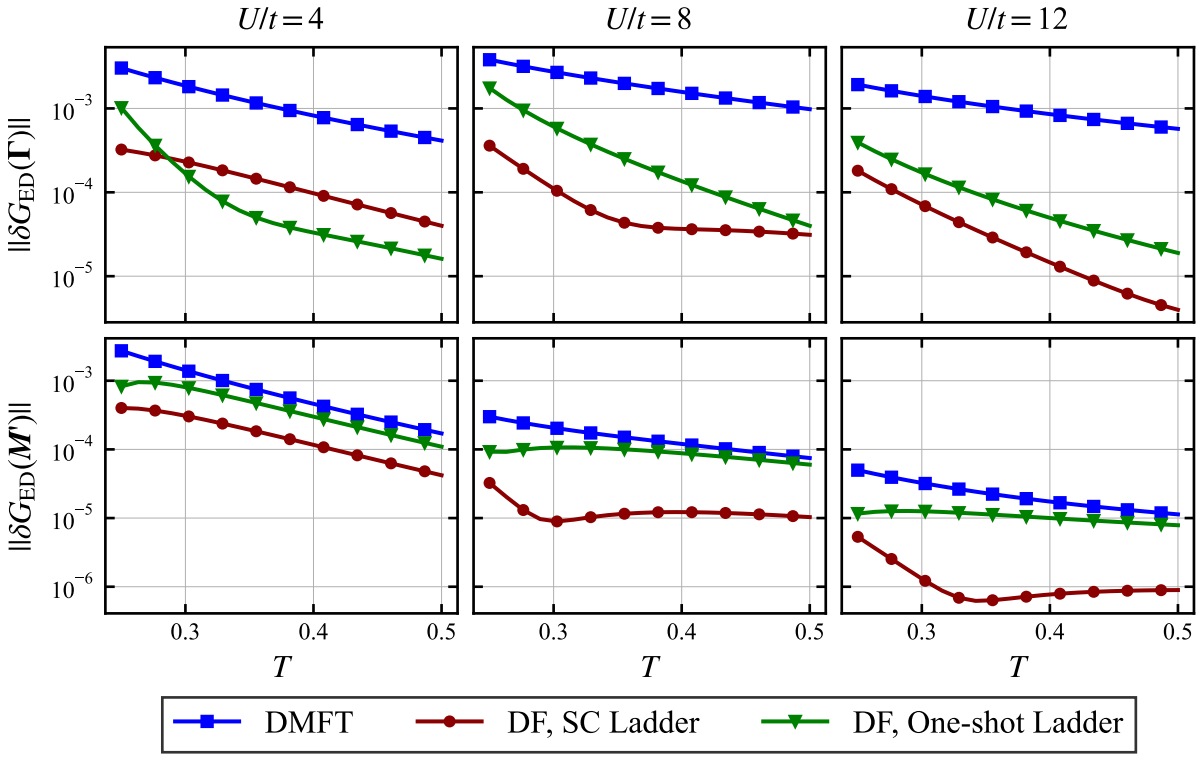

Figure 8: Deviation of the approximate solution from the exact results, measured using the norm defined in Eq. (4.1). The calculations were performed at half filling, $\mu = U/2$, for $\mathbf{k} = \mathbf{\Gamma}$ in the upper panel, and $\mathbf{k} = \boldsymbol{M}'$ in the lower panel.

We first consider the deviation of the approximation schemes at half filling versus temperature, shown in Fig. 8. At $\mathbf{k} = \boldsymbol{M}'$, the results agree well with the expected relative performance of the approximations. The self-consistent ladder performs best, DMFT performs worst, and the one-shot ladder gives intermediate results. As the temperature and interaction strengths are increased, the approximation schemes generally become more accurate. The improved performance at higher temperatures can be attributed to the increased importance of thermal fluctuations, which suppresses nonlocal correlation effects.

At $\mathbf{k} = \mathbf{\Gamma}$ and $U/t = 4$, the one-shot ladder simulations are closer to the exact result than the self-consistent ladder calculation for $T \geq 0.30$. However, this behavior is not observed at other points in the Brillouin zone, nor at larger interaction strengths. The apparent improvement is therefore likely due to accidental error cancellation, rather than a systematic advantage of the one-shot approximation. In particular, considering only a restricted class of diagrams can overemphasize certain effects, while compensating contributions from other diagrams are absent in the approximation. Thus, the self-consistent ladder approach does not necessarily improve agreement with the exact result at every momentum point, especially when neglected diagrams would partially cancel contributions from the considered diagrams.

Outside of the CDW, the approximation schemes are generally expected to perform well in the strongly correlated regime, $U/t \gg 1$. In this limit, hopping is energetically suppressed and the system is driven towards the atomic limit, so local physics is expected to dominate, making DMFT a suitable starting point [14]. Consistent with this expectation, the approximation schemes generally perform better at $U/t = 12$, than in the moderately to strongly correlated regime, $U/t = 8$. At $\mathbf{k} = \mathbf{\Gamma}$, the approximation schemes generally perform worst at $U/t = 8$, which appears to be a particularly difficult regime, possibly attributed to the simultaneous importance of local and nonlocal effects.

4.1.2 Comparison with Exact Diagonalization away from Half Filling

Half filling is a special point in phase space due to particle-hole symmetry. It is therefore important to examine the performance of the approximation schemes away from this point, illustrated in Fig. 9. As mentioned in Sec. 2.6.3, away from half filling, higher-order impurity vertex functions no longer vanish. However, the diagrammatic selection considered here includes only the second-order impurity vertex, even away from half filling.

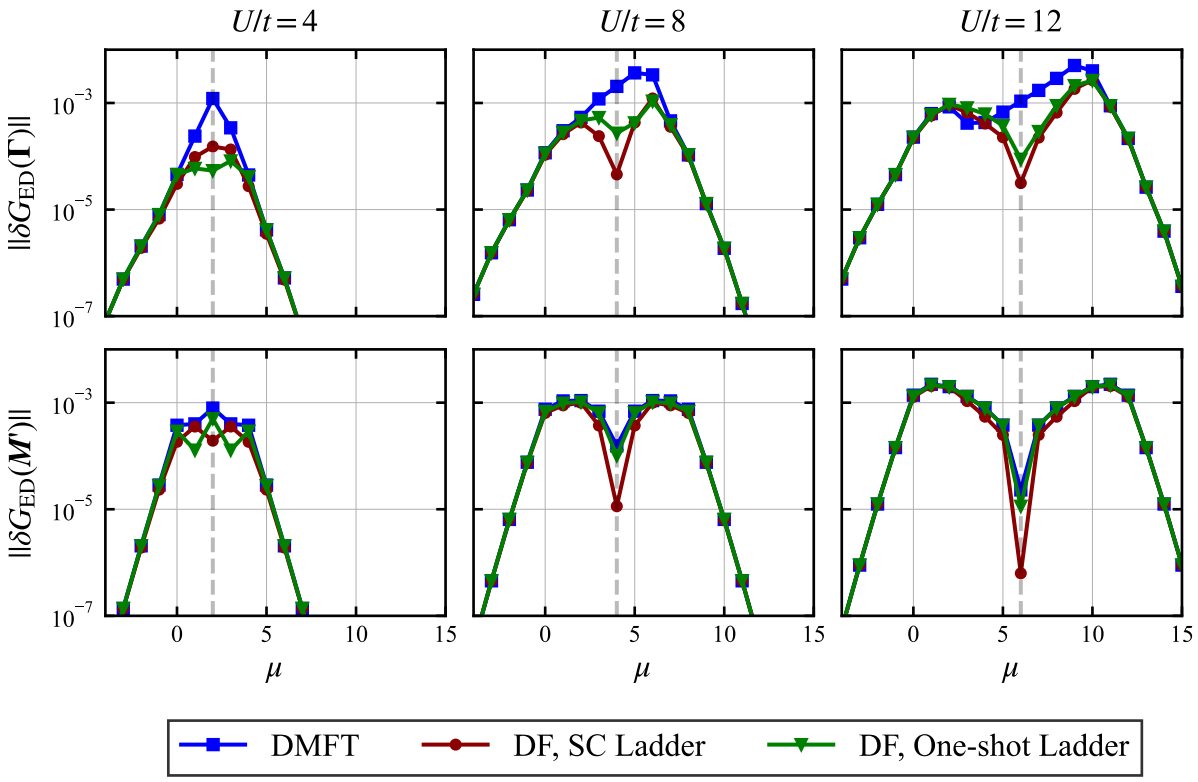

Figure 9: Deviation of the approximate solution from the exact results, measured using the norm defined in Eq. (4.1), against chemical potential μ. The dashed vertical line marks half filling, $\mu = U/2$. The calculations were performed at $T = 0.35$ for $\mathbf{k} = \mathbf{\Gamma}$ in the upper panel, and $\mathbf{k} = \boldsymbol{M}'$ in the lower panel.

Comparisons based on scans over μ are more difficult, since the electron density changes along the scan. Focusing on the $\boldsymbol{M}'$ point, the self-consistent ladder approach obtains a local

minima at half filling. This is expected, as the approximation scheme is most accurate at this point. Away from half filling, the dual-fermion approximation schemes perform worse, which can be attributed to the fact that higher-order impurity vertex functions are no longer identically zero, meaning the diagrammatic selection is further from the exact results. In the strongly doped regimes, corresponding to chemical potentials that drive the system far away from half-filling, the approximation schemes all perform similarly. This can be understood from the limited number of possible configurations at very low or very high electron densities, which makes the physics comparatively simple. Intermediate doping away from half filling is more nontrivial and highly momentum dependent, as indicated by the corresponding results at the $\mathbf{\Gamma}$-point.

4.1.3 Convergence at Half Filling

The half-filled Falicov–Kimball system at $U/t \approx 4$ lies within the Anderson insulating phase[20], where effective disorder arising from thermal averaging over f-electron configurations becomes important [49, 72]. In this regime, convergence of the self-consistent ladder simulations is comparatively slow, illustrated in Fig. 10. Outside the CDW phase and away from the Anderson insulating region, however, convergence typically requires approximately 10 outer-loop iterations for the default parameters considered. This demonstrates that the chosen self-consistency parameters are sufficient to achieve convergence.

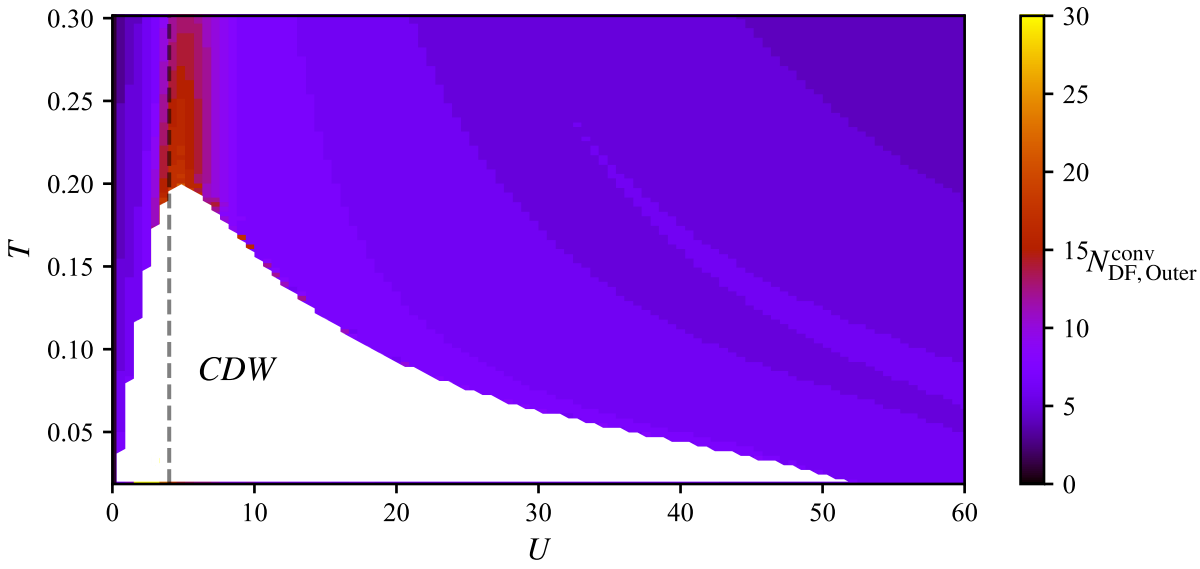

Figure 10: $T-U$ parameter-space diagram at half filling of the number of outer dual-fermion loops required to reach convergence, $N^{\text{conv}}_{\text{DF,Outer}}$. The dotted line marks $U = 4$.

A possible explanation for the slow convergence in the Anderson insulating regime is that this regime is governed by spatially inhomogeneous disorder effects. Since single-site DMFT treats the system as translationally invariant sites coupled to local baths, it does not capture

[20] Recall that we set the hopping parameter to unit, $U/t = U$.

these nonlocal disorder and localization effects. The resulting DMFT solution may therefore provide a less suitable starting point for the dual-fermion ladder calculations, requiring additional self-consistency iterations to reach convergence.

4.1.4 Convergence of Finite Truncation BSE to Ladder BSE

It is useful to examine how the dual-fermion Green's function, obtained from a finite-order truncation of the BSE, converges to the full ladder result. We define the deviation from the ladder solution as $\delta G_{\text{Ladder}}(\mathbf{k},\nu) = G_{\text{Ladder}}(\mathbf{k},\nu) - G_{\text{Truncated BSE}}(\mathbf{k},\nu)$, and use the norm introduced in Eq. (4.1) to quantify convergence. We focus on one-shot calculations, since the self-consistent results were found to be qualitatively similar.

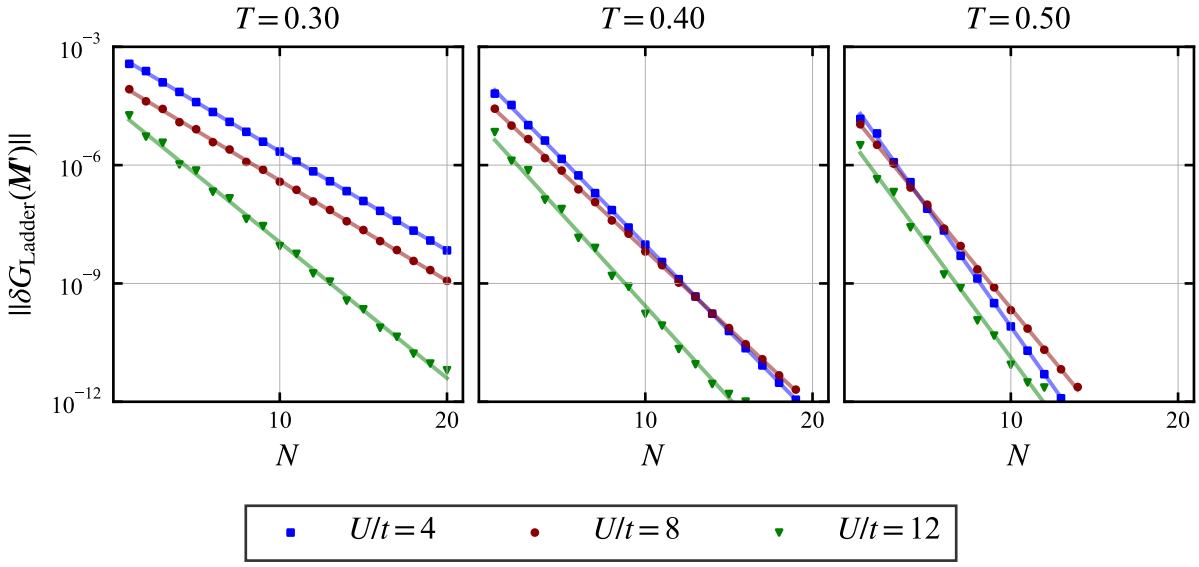

Figure 11: Deviation from the full ladder solution as a function of the impurity-vertex order N at which the BSE is truncated, evaluated at $\mathbf{k} = \boldsymbol{M}'$ for half filling. The lines are fits of the form $||\delta G_{\text{ladder}}|| = CB^N$, with C and B determined from the fit.

In Fig. 11, we observe that the convergence generally increases at higher temperatures and correlation strengths. At $\mathbf{k} = \boldsymbol{\Gamma}$, however, convergence was found to be slowest at $U/t = 8$. The fitting model is motivated by the structure of the renormalized dual vertex function, which has the form $\tilde{\Gamma} \sim (1 - B)^{-1}$. A finite-order truncation of the ladder corresponds to truncating this geometric series at order N. The leading truncation error is therefore expected to scale as $\delta G(\mathbf{k}) \sim B^N$. In principle, the error receives contributions from several momentum channels. A more constrained fitting form is therefore

$$||\delta G_{\text{ladder}}(\mathbf{k})|| = \sum_{\mathbf{q}} C_{\mathbf{q}} B(\mathbf{q})^N, \tag{4.2}$$

where the values of $B(\mathbf{q})$ are fixed from the dual-fermion calculation and only the amplitudes $C_{\mathbf{q}}$ are fitted. In practice, this fit becomes numerically unstable at small norms. We therefore use the single exponential fit, and subsequently compare the fitted value of B with the values

of $B(\mathbf{q})$ obtained from the dual-fermion calculations. For the considered parameter range, the fitted value of B was found to be closest to $B(\mathbf{q})$ at $\mathbf{q} = \boldsymbol{M}'$ throughout. The relative difference, $|B(\boldsymbol{M}') - B_{\text{fit}}||B(\boldsymbol{M}')|^{-1}$ ranges from approximately 6% to 27% for the performed fits.

4.2 The Pick Matrix for Causal Systems - Analytical Results

4.2.1 Exact Green's Function

We consider the Pick matrix constructed from the analytic expression for the exact Green's function in Eq. (2.5),

$$\mathscr{G}(\mathbf{k}, z) = \sum_{l}^{M} \frac{a_l(\mathbf{k})}{z - \omega_l}, \tag{4.3}$$

where l denotes the combined index (m, n), $a_l \in \mathbb{R} > 0$ are the spectral weights of the Green's function, and $\omega_l \in \mathbb{R}$ are the corresponding transition energies. For N interpolation nodes, we define the vector $\mathbf{Q}_l = ([z_0 - \omega_l]^{-1}, \ldots, [z_{N-1} - \omega_l]^{-1})$, from which the Pick matrix can be written as[21]

$$P_{ij}[G] = \sum_{l}^{M} a_l(\mathbf{k})(\mathbf{Q}_l)_i(\mathbf{Q}_l^\dagger)_j \Rightarrow P = \sum_{l}^{M} a_l(\mathbf{k})\mathbf{Q}_l\mathbf{Q}_l^\dagger = Q\text{diag}(a)Q^\dagger. \tag{4.4}$$

Here, we introduced the $N \times M$ matrix quantity $Q = [\mathbf{Q}_0, \ldots \mathbf{Q}_M]$, whose columns are the vectors $\mathbf{Q}_l$, and the $M \times M$ diagonal matrix $\text{diag}(a)$, with the spectral weights a_l on the diagonal. Thus, the Pick matrix is a rectangular congruence transformation of the spectral weights. If all of the spectral weights are positive, the Pick matrix is trivially PSD.

The matrix $Q_{ij} = (z_i - \omega_j)^{-1}$ is a Cauchy matrix [73]. Any $n \times n$ square submatrix of Q has determinant

$$\det Q_{n\times n} = \frac{\prod_{i>j}^{n}(z_i - z_j)(\omega_j - \omega_i)}{\prod_{i,j}^{n}(z_i - \omega_j)}. \tag{4.5}$$

The poles ω_l are real and distinct,[22] while the interpolation nodes $z_i \in \mathbb{C}^+$ are also distinct by assumption (See Theorem 3). Hence, no factor in the numerator or the denominator of Eq. (4.5) vanishes, and every square submatrix of Q has a nonzero determinant.[23] Since the rank of a matrix is the size of its largest nonsingular square submatrix [74], we obtain that $\text{rank}Q = \min(N, M) = \text{rank}P$, where the last equality follows by the assumption that the spectral weights are nonzero. Moreover, since the rank of a Hermitian matrix is the number of nonzero eigenvalues[24], we have proved the following theorem:

[21] See the appendix for a short proof.
[22] If the sum in Eq. (4.3) contains repeated poles, their spectral weights can be combined.
[23] Any submatrix of a Cauchy matrix is also a Cauchy matrix.
[24] This follows immediately from the singular value decomposition.

Theorem 4. The number of nonzero eigenvalues of the Pick matrix in Eq. (4.4) is $\min(N, M)$, where N denotes the number of interpolation nodes and M the number of poles, which are assumed to be distinct and to have nonzero spectral weights.

If Q is square, it follows by Sylvester's law of inertia [33] that all spectral weights are necessarily positive if the Pick matrix is PSD. If Q is rectangular, however, we must use the following generalization of Sylvester's law of inertia [75, Lemma 2],

Theorem 5. Let $i_{\pm}(D)$ denote the number of positive or negative eigenvalues of the Hermitian matrix $D \in \mathbb{C}^{M\times M}$. For any matrix $Q^{\dagger} \in \mathbb{C}^{M\times N}$ of rank r,

$$i_{\pm}(D) - (M - r) \leq i_{\pm}(QDQ^{\dagger}) \leq i_{\pm}(D). \tag{4.6}$$

If the Pick matrix is PSD, it has no negative eigenvalues, meaning that $i_{-}(Q\mathrm{diag}(a)Q^{\dagger}) = 0$. Moreover, since $r = \min(N, M)$, this becomes $i_{-}(\mathrm{diag}(a)) \leq M - N$ provided $M > N$. Thus, if the number of poles exceeds the number of interpolation nodes, the Pick criterion may be satisfied even though some of the spectral weights are negative[25]. However, all spectral weights are guaranteed to be positive provided that the number of interpolation nodes exceeds the number of poles, $N > M$. See Sec. 6.1.3 of the Appendix, where these formulas are applied to the noninteracting limit, allowing for further analytical simplifications.

4.3 Causality in the Dual-Fermion Approach

To investigate causality within the ladder dual-fermion approach, initial parameter-space scans were performed on 4×4 systems. Parameter regimes in which large negative Pick eigenvalues were observed were subsequently compared with ED and DMFT results, and then re-examined on larger lattices to assess finite-size effects. As expected, no large negative Pick eigenvalues were found in parameter-space scans based on DMFT Green's functions. All dual-fermion Green's functions are computed using the full ladder resummation of the BSE unless otherwise stated.

4.3.1 Causality at Half Filling

As displayed in Figs. 12 and 13, large negative Pick eigenvalues are observed close to the CDW phase boundary at half filling, both in the one-shot and self-consistent simulations. These eigenvalues are associated with the dual vertex function becoming nearly singular, $\tilde{\Gamma} \sim (1 - B)^{-1}$. Consequently, causality violations observed in this regime should be interpreted with caution, since the near-singular vertex may amplify numerical errors. They therefore do not, by themselves, provide robust evidence that the approximation scheme is intrinsically noncausal. More conclusive evidence would require similar violations in parameter regimes where such numerical instabilities are absent.

[25] Since Q has a particular structure, additional constraints may further restrict this possibility.

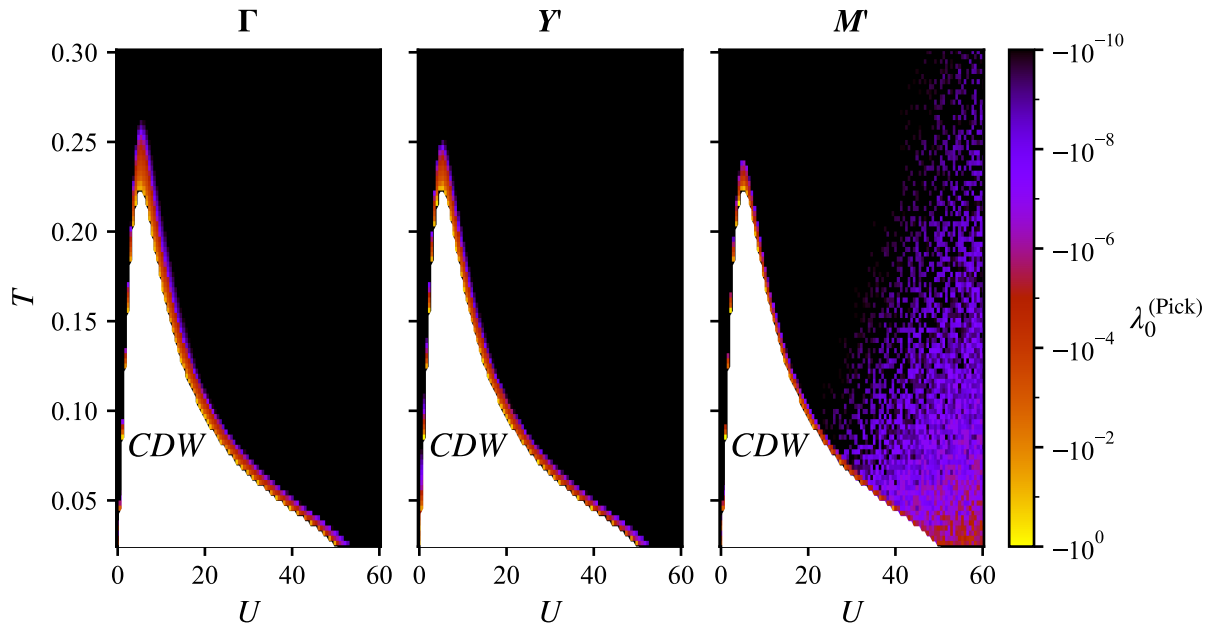

Figure 12: $T-U$ parameter-space diagram of the minimum Pick eigenvalues, $\lambda_0^{(\mathrm{Pick})}$, obtained from one-shot dual-fermion simulations for $L = 4$ at half filling. The white region marks the CDW phase.

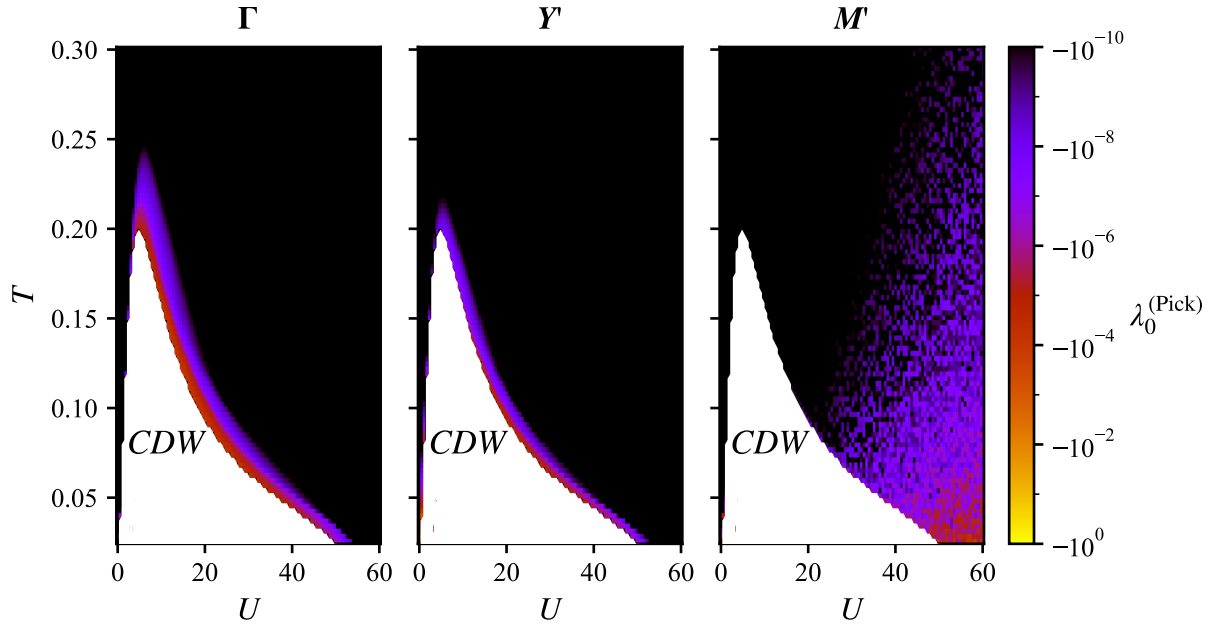

Figure 13: $T-U$ parameter-space diagram of the minimum Pick eigenvalues, $\lambda_0^{(\mathrm{Pick})}$, obtained from self-consistent dual-fermion simulations for $L = 4$ at half filling. The white region marks the CDW phase.

Pick eigenvalues exceeding the established tolerance are observed at the noninteracting Fermi surface, $\mathbf{k} = \boldsymbol{M}'$. Although these deviations occur away from the region of numerical instability, they appear only in the extreme parameter regime $U > 20$. Moreover, the analytical results discussed in Sec. 6.1.3 of the Appendix suggest that a larger Pick eigenvalue tolerance may be needed at the Fermi surface. The large values of U required, together with the possible need for a larger tolerance at the Fermi surface, make us cautious in interpreting these deviations as genuine causality violations.

The parameter-space diagram for the self-consistent calculations is shown in Fig. 13, which is qualitatively similar to the one-shot results in Fig. 12. Thus, several additional layers of self-consistent updates of both the dual Green's function and the hybridization function do not introduce negative spectral weights or nonanalytic features beyond those already present in the one-shot calculations. This provides evidence that the self-consistency updates preserve causality, both with respect to the analytic structure, as argued in Ref. [5], and with respect to nonnegative spectral weights, as speculated in the same reference.

For the remainder of the results, we focus on the one-shot dual-fermion approach, as the results using the self-consistent dual-fermion simulations are found to be qualitatively similar in terms of Pick eigenvalues.

4.3.2 Causality away from Half Filling

Large negative Pick eigenvalues are found away from half filling when scanning over μ at fixed U/t for the $L = 4$ system. The corresponding $T - \mu$ parameter-space diagram for one-shot calculations is shown in Fig. 14. As discussed in Ref. [44], the CDW phase can persist away from half filling, although the critical temperature is reduced. This behavior is reflected in Fig. 14. Moreover, above some critical chemical potential μ_c, the CDW can no longer be sustained, as noted in Ref. [46].

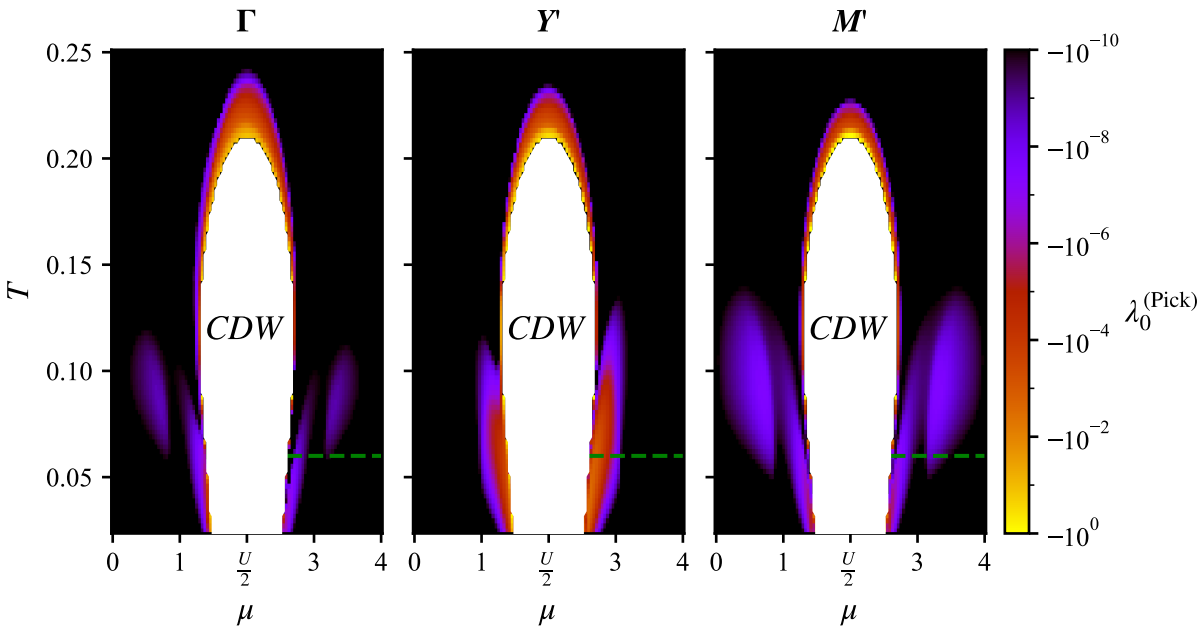

Figure 14: $T-\mu$ parameter-space diagram of the minimum Pick eigenvalues, $\lambda_0^{(\mathrm{Pick})}$, obtained from one-shot dual-fermion simulations at $L = 4$ for $U = 4$. The white region marks the CDW phase. The dashed green line represents the location of the cross section in Fig. 15.

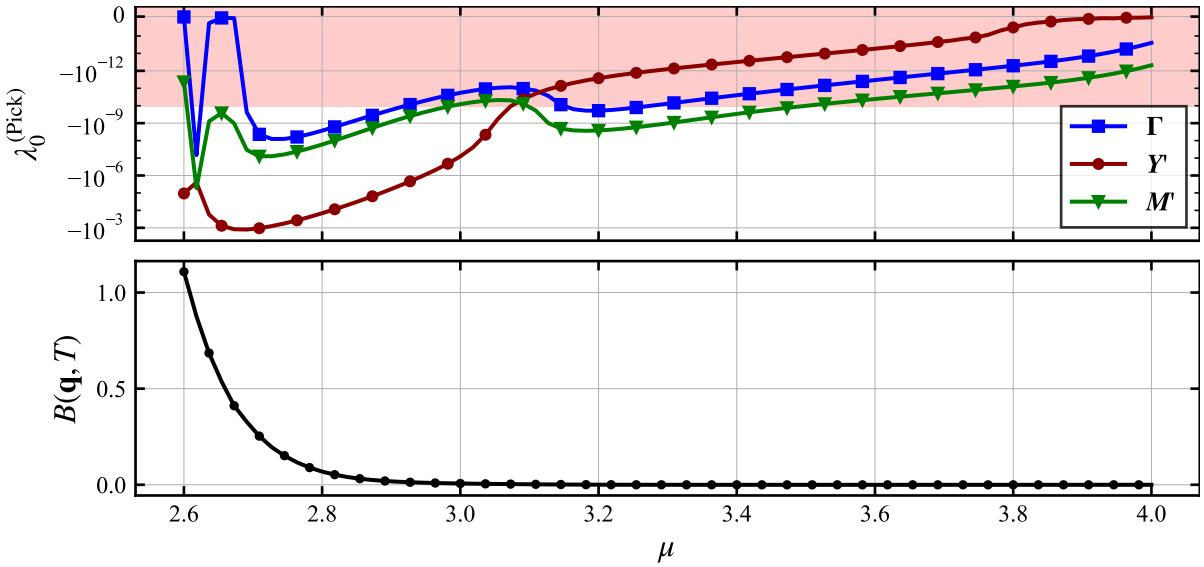

Figure 15: (Top) Cross section of Fig. 14 at $T = 0.06$. The shaded region indicates values below the eigenvalue tolerance, where causality violations cannot be reliably resolved. The cross section is restricted to the region outside the CDW phase, specifically on the right side of half filling. (Bottom) Corresponding $B(\mathbf{q}, T)$ at $\mathbf{q} = (\pi, \pi)$. Values of $B(\mathbf{q}, T)$ in other momentum channels were found to be far away from unity and are therefore omitted.

The region of negative Pick eigenvalues located on the CDW phase boundary for $T \geq 0.15$ in

Fig. 14 is associated with numerical instability. However, the large-magnitude negative Pick eigenvalues observed at the $\boldsymbol{Y}'$-point for $T \leq 0.15$ do not appear to be caused by numerical instabilities.

To investigate the origin of the large negative Pick eigenvalues further, we consider a cross section at $T = 0.06$. This temperature is chosen because it corresponds to the region where some of the largest negative Pick eigenvalues are observed at the $\boldsymbol{Y}'$-point, while still allowing the behavior near the instability region to be resolved. The cross section in Fig. 15 shows that the region of numerical instability is narrow in μ. That is, a small shift in μ produces a relatively large separation from $B(\mathbf{q}, T) = 1$. Consequently, the full ladder solution is accessible at $\mu \approx 2.7$, where $B \approx 0.4$. At this point, no numerical instability associated with the singular behavior $\tilde{\Gamma} \sim (1 - B)^{-1}$ is expected. Nevertheless, the Pick eigenvalue at $\mathbf{k} = \left(0, \frac{\pi}{2}\right)$ is of order $\sim -10^{-3}$, which is well beyond the numerical tolerance and therefore provides strong evidence that the Pick matrix is not PSD. Although this signals genuine causality violations, we do not see this as strong evidence that the dual-fermion approach is noncausal, as this behavior disappears for larger lattice sizes.

To account for the causality violations observed away from half filling and at the noninteracting Fermi surface, we investigated whether the self-energy becomes nearly singular, specifically whether $\tilde{\Sigma}(\mathbf{k}, \nu) g(\nu) \approx -1$ in Eq. (2.46). No such divergence was observed.

4.3.3 Finite Truncation of the BSE

The results discussed in this section have all been in regard to the full ladder resummation of the dual vertex function. To rule out causality violations associated with the full ladder expression, it is useful to consider the effects of truncating the BSE equation to second order in the impurity vertex function, $\tilde{\Gamma} = \gamma + \gamma \tilde{\chi}_0 \gamma$. Indeed, the regions with causality violations observed away from half filling and at the noninteracting Fermi surface persist when the BSE is truncated to second order. The corresponding parameter-space diagrams are shown in Sec. 6.2.2 in the appendix. Hence, the causality violations are not associated with the full ladder resummation. Moreover, truncating the BSE removes the large negative Pick eigenvalues at the phase boundary associated with numerical instabilities, as the dual vertex no longer becomes singular around $B(\mathbf{q}, T) = 1$.

4.3.4 Effects of Interpolation Node Number on the Pick Eigenvalues

As discussed in Sec. 2.3.3, the infinite interpolation-node problem has no solution within the Nevanlinna class if any finite truncation of the Pick matrix has a negative eigenvalue. Consequently, if the Matsubara Green's function yields negative Pick eigenvalues for any finite set of Matsubara frequencies, the Green's function on the full Matsubara grid is guaranteed to be noncausal. It is nonetheless useful to examine the effects of changing the size of the Matsubara grid on the Pick eigenvalues for both causal and noncausal Green's functions.

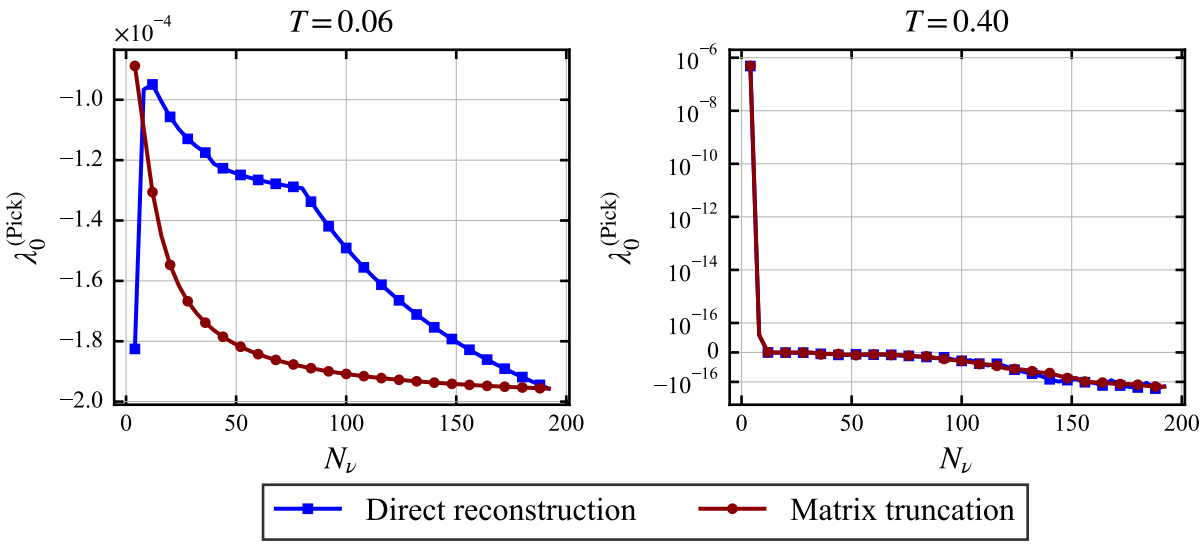

Figure 16: Smallest Pick eigenvalues versus the number of Matsubara frequencies included in the Pick matrix, computed within the one-shot dual-fermion approach. The dotted line shows eigenvalues obtained from submatrices of a Pick matrix constructed using 192-frequency points, while the square markers show results for Green's functions recomputed using the corresponding number of frequencies. Results are shown for $U = 4$, $\mu = 2.8$ and $\mathbf{k} = \boldsymbol{Y}'$ at $L = 4$.

To compute the Pick eigenvalues for smaller Matsubara grids, one may either construct the Pick matrix using the largest chosen number of Matsubara frequencies and then diagonalize its submatrices along the diagonal, or recompute the Green's function using simulations initialized with the corresponding Matsubara grid size. Since the Matsubara grid used to initialize the simulation can affect the resulting Green's function, it is important to check how these two procedures affect the Pick eigenvalues.

The left panel of Fig. 16 shows the minimum Pick eigenvalues in a parameter region where the Pick matrix is not PSD. Using both direct reconstruction and matrix truncation, the Pick eigenvalues remain of the same order of magnitude and generally become more negative as the number of Matsubara frequencies is increased. The fact that a large negative Pick eigenvalue already appears using only four Matsubara frequencies indicates that causality is particularly sensitive to the low-frequency structure of the approximation schemes considered here. This is consistent with the expectation that the approximation schemes considered reproduce the asymptotic high-frequency behavior of the Green's function well, making high-frequency contributions an unlikely source of the observed violations. These observations are, however, specific to the approximation schemes and their implementations considered here.

The right panel of Fig. 16 shows the minimum Pick eigenvalues for parameters corresponding to a causal Green's function. At eight Matsubara frequencies, the eigenvalues decrease to the level of floating-point accuracy, where they remain as the number of Matsubara frequencies is increased in both approaches. The sharp drop from finite values to floating-point values can be understood from the rank of the Pick matrix, derived in Sec. 4.2, namely $\mathrm{rank}(P) =$

$\min(N, M)$. For a small number of interpolation nodes, $\text{rank}(P) = N$, meaning that the Pick matrix has full rank and therefore no zero eigenvalues. Once the number of interpolation nodes exceeds the number of poles, the Pick matrix is no longer of full rank, leading to eigenvalues of floating point magnitude. In general, it is difficult to determine the exact number of poles from the Pick criterion, as the eigenvalues tend to continuously approach finite level precision.

Figure 16 shows that using 96 positive Matsubara frequencies in either approach leads to the same conclusion with regard to causality for both causal and noncausal Green's functions. This justifies the choice of 96 as a default parameter used here. However, for numerical approaches in which the asymptotic form of the Green's function is not well behaved, one should consider increasing the number of positive Matsubara frequencies.

4.3.5 Finite Size Effects

The negative Pick eigenvalues observed away from half filling on the $L = 4$ lattice are not associated with numerical instabilities caused by proximity to the CDW phase boundary, as seen in Fig. 15. These large negative Pick eigenvalues therefore indicate genuine causality violations for this finite system. However, they should not be interpreted as direct evidence that the dual-fermion approach is intrinsically noncausal, since the violations are absent on larger lattices, as shown in panel (b) of Fig. 17.

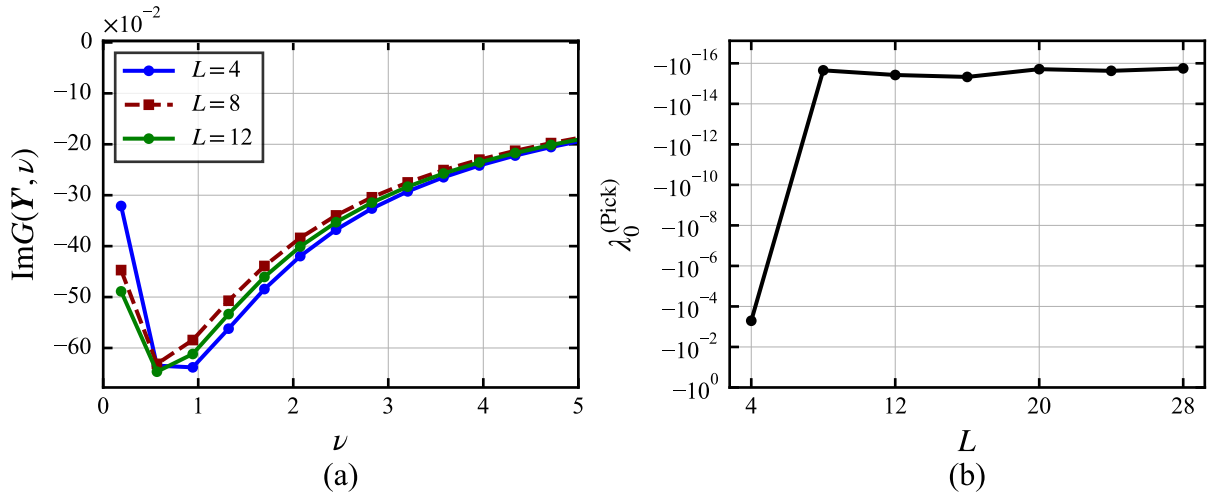

Figure 17: Finite size scaling at $U = 4$, $T = 0.06$ and $\mu = 2.75$ for $\mathbf{k} = \boldsymbol{Y}'$, computed using the one-shot dual-fermion approach. (a) Imaginary part of the Green's function versus Matsubara frequencies. (b) Minimum Pick eigenvalues as a function of system size L.

At the next-largest lattice size for which the point $\mathbf{k} = \boldsymbol{Y}'$ is available, $L = 8$, the large negative Pick eigenvalues are no longer present, as shown in panel (b) of Fig. 17. The main structural change in the Matsubara Green's functions with increasing system size occurs in the first few Matsubara frequencies, as displayed in panel (a) of Fig. 17. Full parameter-space scans of the Pick eigenvalues at $L = 16$ are shown in Sec. 6.2.3 of the appendix.

A proper finite-size analysis should ideally be performed at the $\mathbf{\Gamma}$-point, as it is present for all lattice sizes. Although the Pick eigenvalues at this point, away from the CDW region, remain above the established tolerance, as seen in Fig. 14, their magnitudes are significantly smaller than those observed at other points in the Brillouin zone.

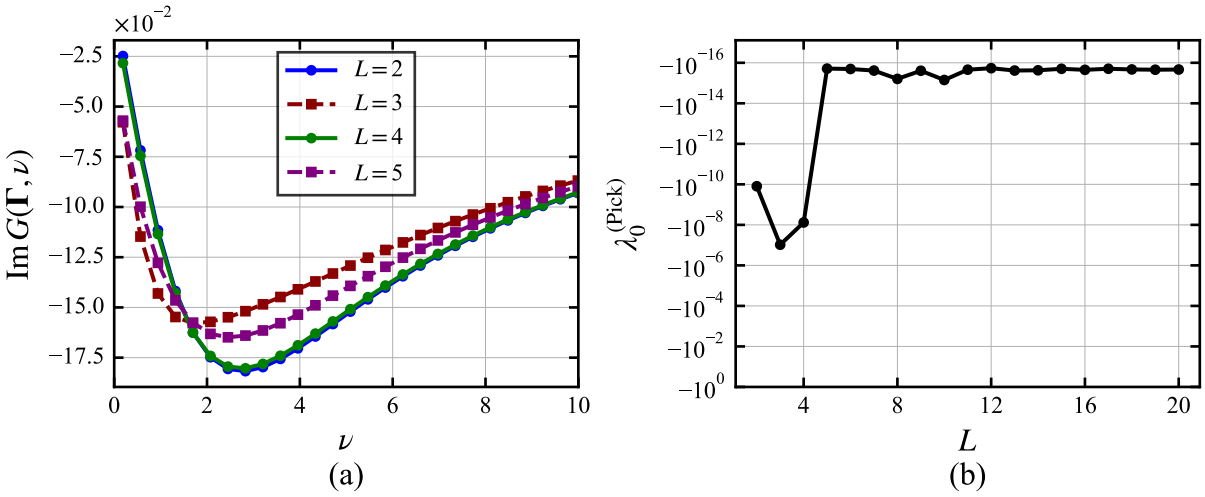

Figure 18: Finite size scaling at $U = 4$, $T = 0.06$ and $\mu = 2.75$ for $\mathbf{k} = \mathbf{\Gamma}$, computed using the one-shot dual-fermion approach. (a) Imaginary part of the Green's function versus Matsubara frequencies. (b) Minimum Pick eigenvalues as a function of system size L.

In panel (b) of Fig. 18, we observe that the large negative Pick eigenvalues disappear between $L = 4$ and $L = 5$. The jump by several orders of magnitude indicates that the large negative Pick eigenvalues observed for $L = 2, 3, 4$ are genuine negative eigenvalues, rather than numerical noise. We also note the oscillatory finite-size behavior of the imaginary part of the Green's function, shown in panel (a) of Fig. 18. This behavior is likely related to the coarse and strongly L-dependent momentum grids of small systems, where changing the lattice size substantially alters the set of available momenta. As the system size is increased and the momentum grid becomes denser, this oscillatory behavior is no longer observed.

From the finite-size analysis, we observe noncausal behavior for lattice sizes $L \leq 4$. This suggests that the dual-fermion approach may perform poorly for very small finite systems. One possible reason for this is that both the dual-fermion approach and DMFT are based on single-site impurity models coupled to self-consistent baths, which more naturally represent environments in the thermodynamic limit, as previously discussed. In contrast, small finite systems retain strong finite-size effects, such as discrete, delta-peaked spectral functions. These effects may therefore lead to a mismatch between the exact finite-size solution and the bath-based description underlying DMFT and the dual-fermion approach.

5 Conclusion

In this work, we elaborated on the Pick formalism as a numerical diagnostic tool for investigating causality of Green's functions. The method was applied to the ladder dual-fermion approach with static scattering only in the spinless Falicov–Kimball model. For small systems, large negative Pick eigenvalues were observed outside of the CDW phase, indicating the presence of causality violations. However, these signals disappeared as the system size was increased. Thus, no robust evidence was found that the dual-fermion approach acts as a causality-violating extension of DMFT. Indeed, it may be the case that the ladder dual-fermion approach is a causal diagrammatic extension of DMFT, or that simplifications specific to the spinless Falicov–Kimball model help preserve causality of the resulting Green's functions. Moreover, the numerical results suggest that self-consistency in the dual-fermion approach preserves causality, since the Pick eigenvalues show no significant differences between one-shot and self-consistent calculations.

Several nontrivial results were obtained in the analysis of the Pick matrix itself. The Pick matrix was shown to be a rectangular congruence transformation of the spectral weights, or residues, of the Green's function under consideration. A connection was also established between the number of nonzero eigenvalues and the number of distinct poles. This may be useful for further analytical studies of the Pick criterion in the context of Green's functions. Although the relation is formally exact, extracting the number of poles from the Pick eigenvalue spectrum is numerically challenging, since eigenvalues lie close to the floating-point precision, making it difficult to differentiate finite eigenvalues from zero. Moreover, the noninteracting Pick eigenvalue spectrum and its eigenvectors were derived, providing a useful benchmark for estimating numerical tolerances and identifying noncausal behavior. However, more established methods of estimating errors of eigenvalues were found to provide stricter tolerances. The analytical result for the noninteracting Pick matrix provides a possible explanation for the noninteracting Fermi surface being particularly susceptible to negative Pick eigenvalues above an established tolerance, as the matrix norm of the Pick matrix is maximal at this point [26].

While the Pick formalism provides a mathematically rigorous causality criterion that is easy to implement, its practical application requires careful tolerance estimates and robustness checks across a wide variety of parameters. Moreover, the Pick criterion is highly sensitive, as a slight change in the input values can alter the eigenvalues significantly. Most data with noise fail the Pick criterion [9], making its application rather limited.

Possible extensions of this work include incorporating dynamic scattering into the BSE and investigating its consequences for causality. Moreover, analytical approaches to the causality of the dual-fermion approximation based on finite-temperature cutting rules, established in Ref. [76] and further developed in Ref. [8] in the context of positive spectral functions, should be explored as a possible route toward a formal proof of spectral positivity.

[26] See Sec. 6.1.3 of the Appendix. This was only verified in the noninteracting limit.

References

[1] P. Hohenberg and W. Kohn, "Inhomogeneous electron gas," *Phys. Rev.*, vol. 136, pp. B864–B871, Nov 1964.

[2] W. Kohn and L. J. Sham, "Self-consistent equations including exchange and correlation effects," *Phys. Rev.*, vol. 140, pp. A1133–A1138, Nov 1965.

[3] A. L. Fetter and J. D. Walecka, *Quantum Theory of Many-Particle Systems*. McGraw-Hill, 1971.

[4] W. Metzner and D. Vollhardt, "Correlated lattice fermions in $d = \infty$ dimensions," *Phys. Rev. Lett.*, vol. 62, pp. 324–327, Jan 1989.

[5] A. N. Rubtsov, M. I. Katsnelson, A. I. Lichtenstein, and A. Georges, "Dual fermion approach to the two-dimensional hubbard model: Antiferromagnetic fluctuations and fermi arcs," *Phys. Rev. B*, vol. 79, p. 045133, Jan 2009.

[6] G. Biroli, O. Parcollet, and G. Kotliar, "Cluster dynamical mean-field theories: Causality and classical limit," *Phys. Rev. B*, vol. 69, p. 205108, May 2004.

[7] M. H. Hettler, A. N. Tahvildar-Zadeh, M. Jarrell, T. Pruschke, and H. R. Krishnamurthy, "Nonlocal dynamical correlations of strongly interacting electron systems," *Phys. Rev. B*, vol. 58, pp. R7475–R7479, Sep 1998.

[8] M. J. Hyrkäs, D. Karlsson, and R. van Leeuwen, "Cutting rules and positivity in finite temperature many-body theory," *Journal of Physics A: Mathematical and Theoretical*, vol. 55, p. 335301, aug 2022.

[9] J. Fei, C.-N. Yeh, and E. Gull, "Nevanlinna analytical continuation," *Phys. Rev. Lett.*, vol. 126, p. 056402, Feb 2021.

[10] G. Pick, "Über die beschränkungen analytischer funktionen, welche durch vorgegebene funktionswerte bewirkt werden," *Mathematische Annalen*, vol. 77, no. 1, pp. 7–23, 1916.

[11] J. B. Garnett, *Bounded Analytic Functions*, vol. 236 of *Graduate Texts in Mathematics*. New York: Springer, revised first edition ed., 2007.

[12] T. Ribic, G. Rohringer, and K. Held, "Nonlocal correlations and spectral properties of the falicov-kimball model," *Phys. Rev. B*, vol. 93, p. 195105, May 2016.

[13] J. K. Freericks and P. Miller, "Dynamical charge susceptibility of the spinless falicov-kimball model," *Physical Review B*, vol. 62, p. 10022–10032, Oct. 2000.

[14] F. Aryasetiawan, *Elements Of Green Function And Density Functional Theory*. Singapore: World Scientific Publishing, Jan. 2025.

[15] A. A. Abrikosov, L. P. Gor'kov, and I. E. Dzyaloshinskii, "On the application of quantum-field-theory methods to problems of quantum statistics at finite temperatures," *Soviet Physics JETP*, vol. 9, pp. 636–641, Sept. 1959. Translated from Zh. Eksp. Teor. Fiz. 36 (1959) 900–908.

[16] P. Coleman, *Introduction to Many-Body Physics*. Cambridge University Press, 2015.

[17] M. Reitner, *Many-electron physics beyond the skeleton series*. Dissertation, Technische Universität Wien, 2025.

[18] T. W. Gamelin, *Complex Analysis*. Undergraduate Texts in Mathematics, Springer-Verlag New York, 2001.

[19] E. C. Titchmarsh, *Introduction to the Theory of Fourier Integrals*. Oxford: Clarendon Press, 2 ed., 1948.

[20] K. F. Riley, M. P. Hobson, and S. J. Bence, *Mathematical Methods for Physics and Engineering: A Comprehensive Guide*. Cambridge University Press, 3 ed., 2006.

[21] S. Backes, J.-H. Sim, and S. Biermann, "Nonlocal correlation effects in fermionic many-body systems: Overcoming the noncausality problem," *Phys. Rev. B*, vol. 105, p. 245115, Jun 2022.

[22] Z. Huang, E. Gull, and L. Lin, "Robust analytic continuation of green's functions via projection, pole estimation, and semidefinite relaxation," *Phys. Rev. B*, vol. 107, p. 075151, Feb 2023.

[23] L. N. Trefethen, "Quantifying the ill-conditioning of analytic continuation," *BIT Numerical Mathematics*, vol. 60, no. 4, pp. 901–915, 2020.

[24] M. Jarrell and J. Gubernatis, "Bayesian inference and the analytic continuation of imaginary-time quantum monte carlo data," *Physics Reports*, vol. 269, no. 3, pp. 133–195, 1996.

[25] G. A. Baker and P. Graves-Morris, *Padé Approximants*. Encyclopedia of Mathematics and its Applications, Cambridge University Press, 2 ed., 1996.

[26] R. K. Bryan, "Maximum entropy analysis of oversampled data problems," *European Biophysics Journal*, vol. 18, pp. 165–174, 1990.

[27] R. Nevanlinna, *Eindeutige analytische Funktionen*, vol. 46 of *Die Grundlehren der mathematischen Wissenschaften in Einzeldarstellungen*. Berlin: Julius Springer, 1936.

[28] J. William F. Donoghue, *Monotone Matrix Functions and Analytic Continuation*, vol. 207 of *Grundlehren der mathematischen Wissenschaften*. Berlin and New York: Springer, 1974.

[29] M. Nedić, "Characterizations of herglotz–nevanlinna functions using positive semidefinite functions and the nevanlinna kernel in several variables," *Complex Analysis and Operator Theory*, vol. 15, p. 109, 2021.

[30] Y. Dyukarev, "The nevanlinna formula for matrix nevanlinna-pick interpolation," *Linear Algebra and its Applications*, vol. 709, pp. 241–270, 2025.

[31] J. Agler and J. E. McCarthy, *Pick Interpolation and Hilbert Function Spaces*, vol. 44 of *Graduate Studies in Mathematics*. American Mathematical Society, 2002.

[32] J. B. Garnett, *Bounded Analytic Functions*, vol. 236 of *Graduate Texts in Mathematics*. New York: Springer, revised first edition ed., 2007.

[33] R. A. Horn and C. R. Johnson, *Matrix Analysis*. Cambridge: Cambridge University Press, 2 ed., 2013.

[34] S. G. Krantz, *Handbook of Complex Variables*. Boston, MA: Birkhäuser Boston, 1999.

[35] D. Fasino and V. Olshevsky, "How bad are symmetric pick matrices?," in *Structured Matrices in Mathematics, Computer Science, and Engineering I*, vol. 280 of *Contemporary Mathematics*, pp. 301–311, American Mathematical Society, 2001.

[36] L. M. Falicov and J. C. Kimball, "Simple model for semiconductor-metal transitions: Smb_6 and transition-metal oxides," *Phys. Rev. Lett.*, vol. 22, pp. 997–999, May 1969.

[37] X.-H. Li, Z. Chen, and T. K. Ng, "Generalized falicov-kimball models," *Phys. Rev. B*, vol. 100, p. 094519, Sep 2019.

[38] V. Turkowski and J. K. Freericks, "Nonequilibrium perturbation theory of the spinless falicov-kimball model: Second-order truncated expansion in u," *Phys. Rev. B*, vol. 75, p. 125110, Mar 2007.

[39] K. W. Becker, S. Sykora, and V. Zlatic, "Static and dynamic properties of the spinless falicov-kimball model," *Phys. Rev. B*, vol. 75, p. 075101, Feb 2007.

[40] J. K. Freericks, C. Gruber, and N. Macris, "Phase separation and the segregation principle in the infinite-u spinless falicov–kimball model," *Physical Review B*, vol. 60, pp. 1617–1626, July 1999.

[41] E. G. C. P. van Loon, *Collective phenomena in strongly correlated systems*. Phd thesis, Radboud University, Nijmegen, The Netherlands, 2018.

[42] J. K. Freericks and V. Zlatić, "Exact dynamical mean-field theory of the falicov-kimball model," *Rev. Mod. Phys.*, vol. 75, pp. 1333–1382, Oct 2003.

[43] U. Brandt and C. Mielsch, "Free energy of the falicov-kimball model in large dimensions," *Zeitschrift für Physik B Condensed Matter*, vol. 82, pp. 37–41, 1991.

[44] A. E. Antipov, E. Gull, and S. Kirchner, "Critical exponents of strongly correlated fermion systems from diagrammatic multiscale methods," *Phys. Rev. Lett.*, vol. 112, p. 226401, Jun 2014.

[45] D. Tong, "Statistical physics." Lecture notes, University of Cambridge. Section 5: Phase Transitions.

[46] A. Mishra, H. U. R. Strand, and E. G. C. P. van Loon, "Benchmarking the dual fermion approach on the falicov-kimball model," 2026.

[47] K. Byczuk, "Metal-insulator transitions in the falicov-kimball model with disorder," *Phys. Rev. B*, vol. 71, p. 205105, May 2005.

[48] Z. Qi, Y. Zhang, M. Qin, H. Weng, and K. Jiang, "Anderson localization: A density matrix approach," *Phys. Rev. X*, vol. 16, p. 011043, Mar 2026.

[49] A. E. Antipov, Y. Javanmard, P. Ribeiro, and S. Kirchner, "Interaction-tuned anderson versus mott localization," *Phys. Rev. Lett.*, vol. 117, p. 146601, Sep 2016.

[50] L. c. v. Frk, P. Baláž, E. Archemashvili, and M. Žonda, "Unsupervised machine learning phase classification for the falicov-kimball model," *Phys. Rev. B*, vol. 111, p. 205116, May 2025.

[51] E. Gull, A. J. Millis, A. I. Lichtenstein, A. N. Rubtsov, M. Troyer, and P. Werner, "Continuous-time monte carlo methods for quantum impurity models," *Rev. Mod. Phys.*, vol. 83, pp. 349–404, May 2011.

[52] P. W. Anderson, "Localized magnetic states in metals," *Phys. Rev.*, vol. 124, pp. 41–53, Oct 1961.

[53] F. B. Anders and G. Czycholl, "X-ray singularities in the f-electron spectral function of the falicov-kimball model," *Phys. Rev. B*, vol. 71, p. 125101, Mar 2005.

[54] J. W. Negele and H. Orland, *Quantum Many-Particle Systems*, vol. 68 of *Frontiers in Physics*. Addison-Wesley Publishing Company, 1988.

[55] R. Mizuno, M. Ochi, and K. Kuroki, "Development of an efficient impurity solver in dynamical mean field theory for multiband systems: Iterative perturbation theory combined with parquet equations," *Phys. Rev. B*, vol. 104, p. 035160, Jul 2021.

[56] U. Brandt and C. Mielsch, "Thermodynamics and correlation functions of the falicov-kimball model in large dimensions," *Zeitschrift für Physik B Condensed Matter*, vol. 75, no. 3, pp. 365–370, 1989.

[57] A. Georges, G. Kotliar, W. Krauth, and M. J. Rozenberg, "Dynamical mean-field theory of strongly correlated fermion systems and the limit of infinite dimensions," *Rev. Mod. Phys.*, vol. 68, pp. 13–125, Jan 1996.

[58] T. Maier, M. Jarrell, T. Pruschke, and M. H. Hettler, "Quantum cluster theories," *Rev. Mod. Phys.*, vol. 77, pp. 1027–1080, Oct 2005.

[59] P. Kappl, M. Wallerberger, J. Kaufmann, M. Pickem, and K. Held, "Statistical error estimates in dynamical mean-field theory and extensions thereof," *Phys. Rev. B*, vol. 102, p. 085124, Aug 2020.

[60] D. C. Cabra, A. Honecker, and P. Pujol, eds., *Modern Theories of Many-Particle Systems in Condensed Matter Physics*, vol. 843 of *Lecture Notes in Physics*. Berlin, Heidelberg: Springer, 2012.

[61] G. Kotliar, S. Y. Savrasov, G. Pálsson, and G. Biroli, "Cellular dynamical mean field approach to strongly correlated systems," *Phys. Rev. Lett.*, vol. 87, p. 186401, Oct 2001.

[62] S. Brener, H. Hafermann, A. N. Rubtsov, M. I. Katsnelson, and A. I. Lichtenstein, "Dual fermion approach to susceptibility of correlated lattice fermions," *Phys. Rev. B*, vol. 77, p. 195105, May 2008.

[63] E. G. C. P. van Loon, M. I. Katsnelson, and H. Hafermann, "Second-order dual fermion approach to the mott transition in the two-dimensional hubbard model," *Phys. Rev. B*, vol. 98, p. 155117, Oct 2018.

[64] R. Kubo, "Generalized cumulant expansion method," *Journal of the Physical Society of Japan*, vol. 17, pp. 1100–1120, July 1962.

[65] J. Otsuki, H. Hafermann, and A. I. Lichtenstein, "Superconductivity, antiferromagnetism, and phase separation in the two-dimensional hubbard model: A dual-fermion approach," *Phys. Rev. B*, vol. 90, p. 235132, Dec 2014.

[66] E. G. C. P. van Loon, A. I. Lichtenstein, M. I. Katsnelson, O. Parcollet, and H. Hafermann, "Beyond extended dynamical mean-field theory: Dual boson approach to the two-dimensional extended hubbard model," *Phys. Rev. B*, vol. 90, p. 235135, Dec 2014.

[67] G. Rohringer, H. Hafermann, A. Toschi, A. A. Katanin, A. E. Antipov, M. I. Katsnelson, A. I. Lichtenstein, A. N. Rubtsov, and K. Held, "Diagrammatic routes to nonlocal correlations beyond dynamical mean field theory," *Rev. Mod. Phys.*, vol. 90, p. 025003, May 2018.

[68] G. Rohringer, H. Hafermann, A. Toschi, A. A. Katanin, A. E. Antipov, M. I. Katsnelson, A. I. Lichtenstein, A. N. Rubtsov, and K. Held, "Diagrammatic routes to nonlocal correlations beyond dynamical mean field theory," *Rev. Mod. Phys.*, vol. 90, p. 025003, May 2018.

[69] H. Hafermann, G. Li, A. N. Rubtsov, M. I. Katsnelson, A. I. Lichtenstein, and H. Monien, "Efficient perturbation theory for quantum lattice models," *Phys. Rev. Lett.*, vol. 102, p. 206401, May 2009.

[70] A. E. Antipov, J. P. LeBlanc, and E. Gull, "Opendf - an implementation of the dual fermion method for strongly correlated systems," *Physics Procedia*, vol. 68, p. 43–51, 2015.

[71] J. Barlow and J. Demmel, "Computing accurate eigensystems of scaled diagonally dominant matrices," *SIAM Journal on Numerical Analysis*, vol. 27, no. 3, pp. 762–791, 1990.

[72] L. c. v. Frk, P. Baláž, E. Archemashvili, and M. Žonda, "Unsupervised machine learning phase classification for the falicov-kimball model," *Phys. Rev. B*, vol. 111, p. 205116, May 2025.

[73] A. Pinkus, *Totally Positive Matrices*, vol. 181 of *Cambridge Tracts in Mathematics*. Cambridge: Cambridge University Press, 2010.

[74] P. M. Cohn, *Algebra. Volume 1*. Chichester: John Wiley & Sons, 2 ed., 1982.

[75] C. Paige, G. P. H. Styan, B.-Y. Wang, and F. Zhang, "Hua's matrix equality and schur complements," *International Journal of Information and Systems Sciences*, vol. 3, no. 1, pp. 1–18, 2007.

[76] R. L. Kobes and G. W. Semenoff, "Discontinuities of green functions in field theory at finite temperature and density," *Nuclear Physics B*, vol. 260, pp. 714–746, 1985.

6 Appendix

6.1 Properties of the Pick Matrix

6.1.1 Nevanlinna-Pick Matrix

The Pick criterion can be used to formulate a necessary condition for the existence of a Nevanlinna interpolant using the Cayley transform, as described in Sec. 2.3.3 of the main text, where the Pick matrix is given by

$$\mathcal{P}_{mn}[f] = \frac{1 - \mathscr{C}(f_m)\mathscr{C}(f_n)^*}{1 - \mathscr{C}(z_m)\mathscr{C}(z_n)^*} \quad , \quad \mathscr{C}(z) = \frac{z - i}{z + i} \tag{6.1}$$

Consider the following transformation of a complex vector $\mathbf{z}$,

$$\mathcal{M}_{mn}(\mathbf{z}) = 1 - \mathscr{C}(z_m)\mathscr{C}(z_n)^* = \frac{2i(z_n^* - z_m)}{(z_m + i)(z_n^* - i)} \tag{6.2}$$

Suppose we are considering the Pick matrix for the interpolation problem $f(z_i) = f_i$. Then, the Pick matrix is given by

$$\mathcal{P}_{mn}[f] = \frac{1 - \mathscr{C}(f_m)\mathscr{C}(f_n)^*}{1 - \mathscr{C}(z_m)\mathscr{C}(z_n)^*} \tag{6.3}$$

$$= \frac{(z_m + i)}{(f_m + i)} \frac{(f_m - f_n^*)}{(z_m - z_n^*)} \frac{(z_n^* - i)}{(f_n^* - i)} \tag{6.4}$$

$$= x_m P_{mn} x_n^* \tag{6.5}$$

where we defined the quantities

$$x_m = \frac{(z_m + i)}{(f_m + i)} \quad , \quad P_{mn} = \frac{(f_m - f_n^*)}{(z_m - z_n^*)} \tag{6.6}$$

It is convenient to write this as a matrix equation,

$$\mathcal{P}_{mn} = \sum_{ij} (x_m \delta_{mi}) P_{ij} (x_j^* \delta_{jn}) \iff \mathcal{P} = DPD^\dagger \tag{6.7}$$

where $D = \mathrm{diag}(\mathbf{x})$. Now, let $\mathbf{u}$ be an arbitrary vector in $\mathbb{C}^n$,

$$\mathbf{u}^\dagger \mathcal{P} \mathbf{u} = \mathbf{u}^\dagger D P D^\dagger \mathbf{u} \overset{\mathbf{v}=D^\dagger \mathbf{u}}{=} \mathbf{v}^\dagger P \mathbf{v} \tag{6.8}$$

Provided D has full rank, this proves that $\mathcal{P}$ and P has the same definiteness since $\mathbf{u}$ and $\mathbf{v}$ are arbitrary and can always be constructed from each other. Applying Eq. (6.6) to the Pick matrix in Eq. (6.1),

$$P_{mn}[G] = i \frac{G_m - G_n^*}{\nu_m + \nu_n}. \tag{6.9}$$

6.1.2 Computations for the Pick Matrix of the Exact Green's Function

Consider the Green's function

$$G(\mathbf{k}, z) = \sum_l \frac{a_l(\mathbf{k})}{z - \omega_l}. \tag{6.10}$$

Assuming the spectral weights $a_l(\mathbf{k})$ and the transition energies ω_l are real,

$$G_m - G_n^* = \sum_l a_l(\mathbf{k}) \left[\frac{1}{z_m - \omega_l} - \frac{1}{z_n^* - \omega_l} \right] = -\sum_l a_l(\mathbf{k}) \frac{z_m - z_n^*}{(z_m - \omega_l)(z_n^* - \omega_l)} \tag{6.11}$$

Since the negative Green's function has Nevanlinna structure,

$$P_{mn} = -\frac{G_m - G_n^*}{z_m - z_n^*} = \sum_l a_l(\mathbf{k}) \frac{1}{(z_m - \omega_l)(z_n^* - \omega_l)} = \sum_l a_l(\mathbf{k}) (\mathbf{Q}_l)_m (\mathbf{Q}_l^\dagger)_n, \tag{6.12}$$

which is the expression from the main text.

6.1.3 Noninteracting Limit

We can apply Eq. (4.4) to the noninteracting Green's function, as it has a single pole located at $\omega = \varepsilon(\mathbf{k}) - \mu$ with unit residue. Hence, the Pick matrix takes a particularly simple form[27],

$$P = \mathbf{Q}_0 \mathbf{Q}_0^\dagger \quad , \quad (\mathbf{Q}_0)_n = \frac{1}{i\nu_n - (\varepsilon(\mathbf{k}) - \mu)} = G_0(\mathbf{k}, \nu_n). \tag{6.13}$$

Since the spectral weight of the single pole is positive, the Pick matrix is PSD as expected, as the noninteracting Green's function is causal. Moreover, by Theorem 4, there is only a single nonzero eigenvalue. The eigenvector of the Pick matrix with the nontrivial eigenvalue is clearly $\mathbf{Q}_0$, and the corresponding eigenvalue is the magnitude of the noninteracting Green's function,

$$P\mathbf{Q}_0 = ||\mathbf{Q}_0||^2 \mathbf{Q}_0 \quad , \quad ||\mathbf{Q}_0||^2 = \sum_{n=0}^{N} \frac{1}{\nu_n^2 + (\varepsilon(\mathbf{k}) - \mu)^2} \overset{N\to\infty}{=} \frac{\beta}{4[\varepsilon(\mathbf{k}) - \mu]} \tanh\left(\frac{\beta[\varepsilon(\mathbf{k}) - \mu]}{2} \right). \tag{6.14}$$

At the noninteracting Fermi surface, $\varepsilon(\mathbf{k}) = \mu$, the magnitude of the nonzero Pick eigenvalue is maximal and takes the value $||\mathbf{G}_0||^2 = \frac{\beta^2}{8}$. According to the error bound estimation in Eq. (3.2), this implies that a stricter tolerance on the Pick eigenvalues is generally required near the noninteracting Fermi surface. Consequently, fluctuations around the chosen tolerance near the Fermi surface must be examined in greater detail.

Since the smallest Pick eigenvalue is zero in the noninteracting limit, this limit can be used as an initial estimate for a numerical tolerance that distinguishes genuine causality violations from noise-induced negative Pick eigenvalues. However, more established methods for constructing eigenvalue error bounds, such as the one discussed in Sec. 3.3, generally lead to stricter tolerances.

[27] We explicitly set the interpolation nodes to be the Matsubara frequencies here.

6.2 Additional Results

6.2.1 CDW Instability away from Half Filling

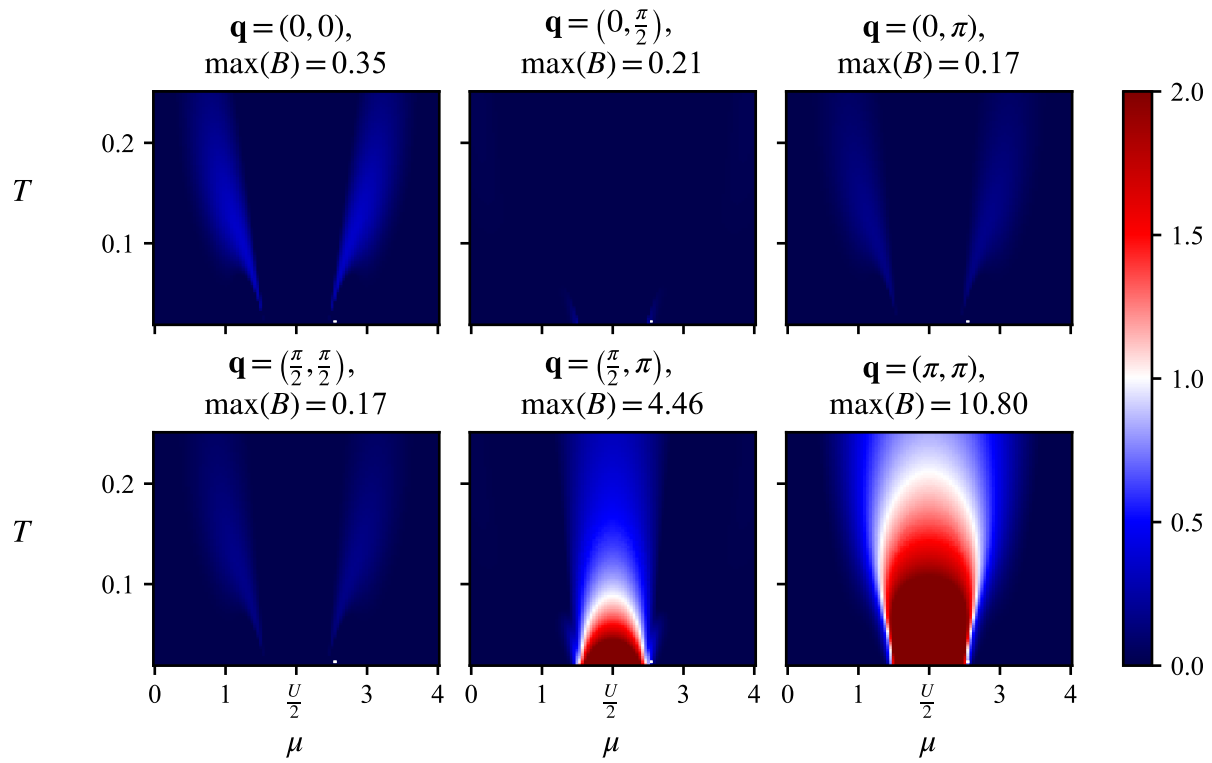

Figure 19: $T - \mu$ parameter-space diagrams of $B(\mathbf{q}, T)$ at $U = 4$, indicating the CDW region away from half filling, computed using the one-shot dual-fermion approach.

6.2.2 Finite Truncation of the BSE

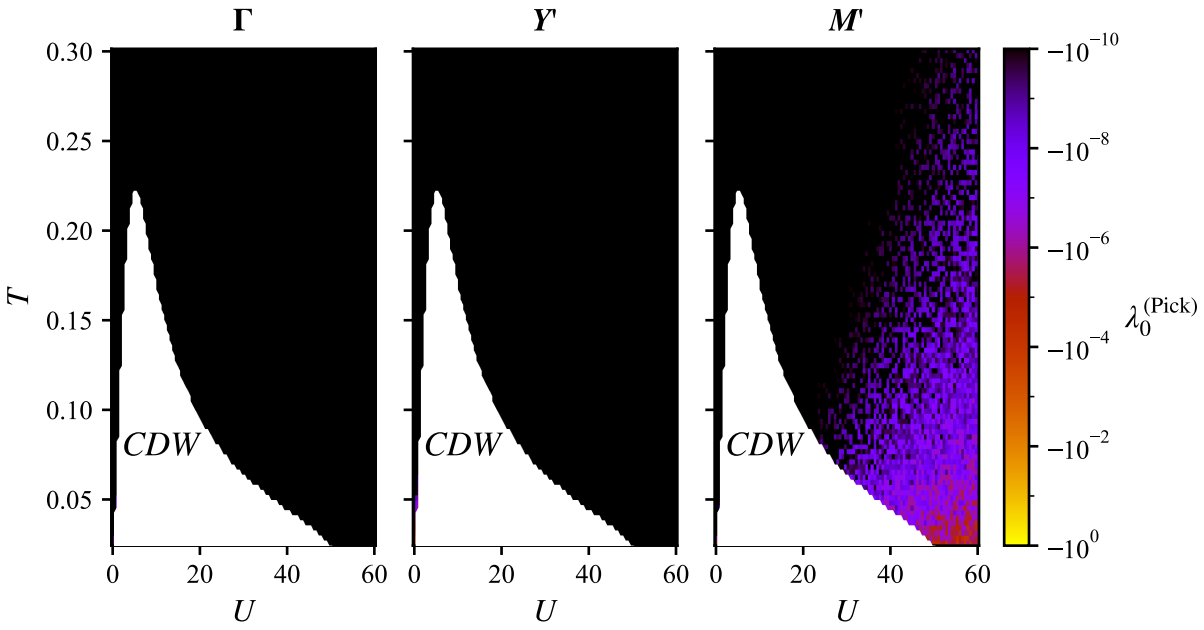

Figure 20: $T-U$ parameter-space diagram of the minimum Pick eigenvalues, $\lambda_0^{(\mathrm{Pick})}$, obtained from one-shot dual-fermion simulations for $L = 4$ at half filling when truncating the BSE to second order in the impurity vertex function, $\tilde{\Gamma} = \gamma + \gamma\tilde{\chi}_0\gamma$. The white region marks the CDW phase.

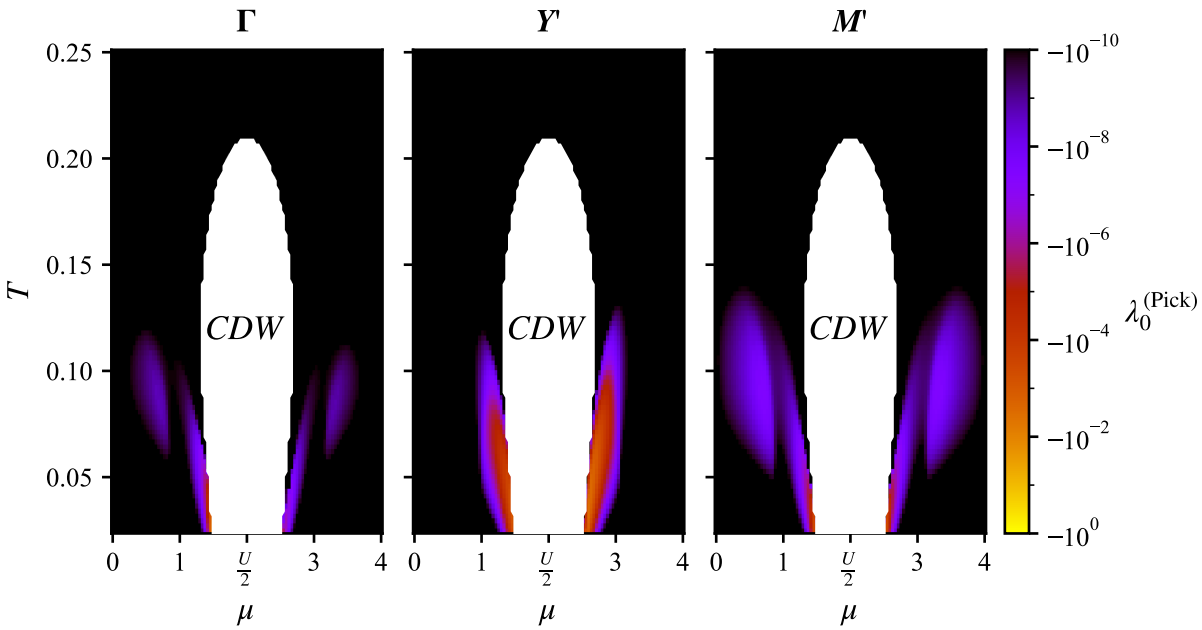

Figure 21: $T-\mu$ parameter-space diagram of the minimum Pick eigenvalues, $\lambda_0^{(\mathrm{Pick})}$, obtained from one-shot dual-fermion simulations for $L = 4$ at $U = 4$ when truncating the BSE to second order in the impurity vertex function, $\tilde{\Gamma} = \gamma + \gamma\tilde{\chi}_0\gamma$. The white region marks the CDW phase.

6.2.3 Parameter-Space Diagrams at $L = 16$

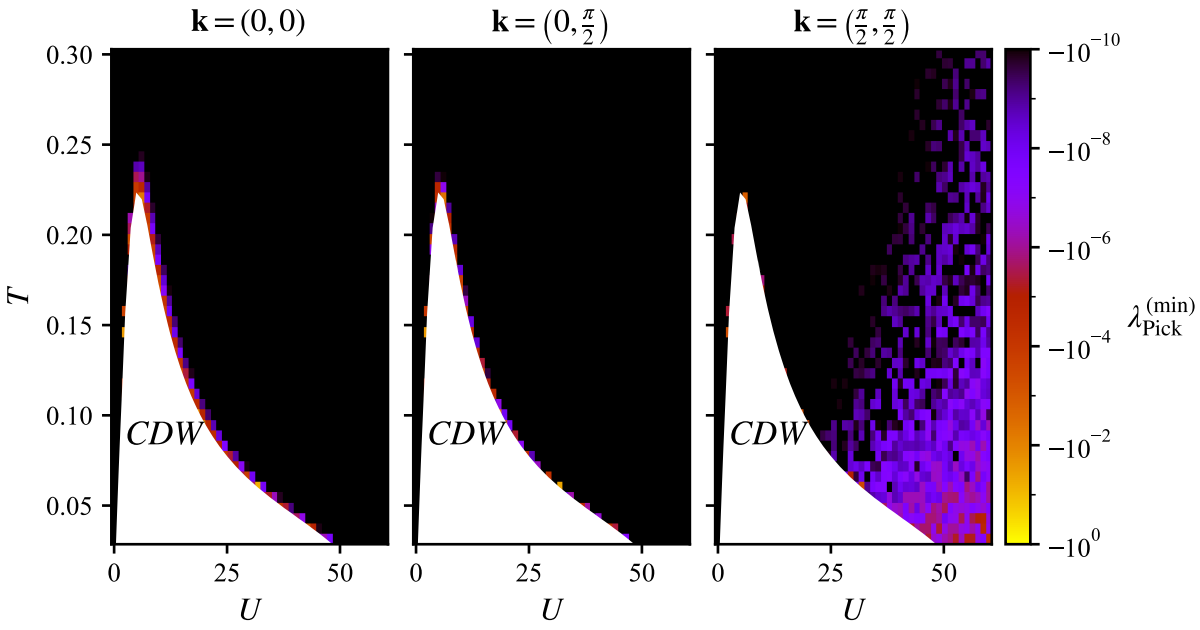

Figure 22: $T - U$ parameter-space diagram of the minimum Pick eigenvalues, $\lambda_{\text{Pick}}^{\text{min}}$, obtained from one-shot dual-fermion simulations for $L = 16$ at half filling using the full ladder resummation of the BSE. The white region marks the CDW phase.

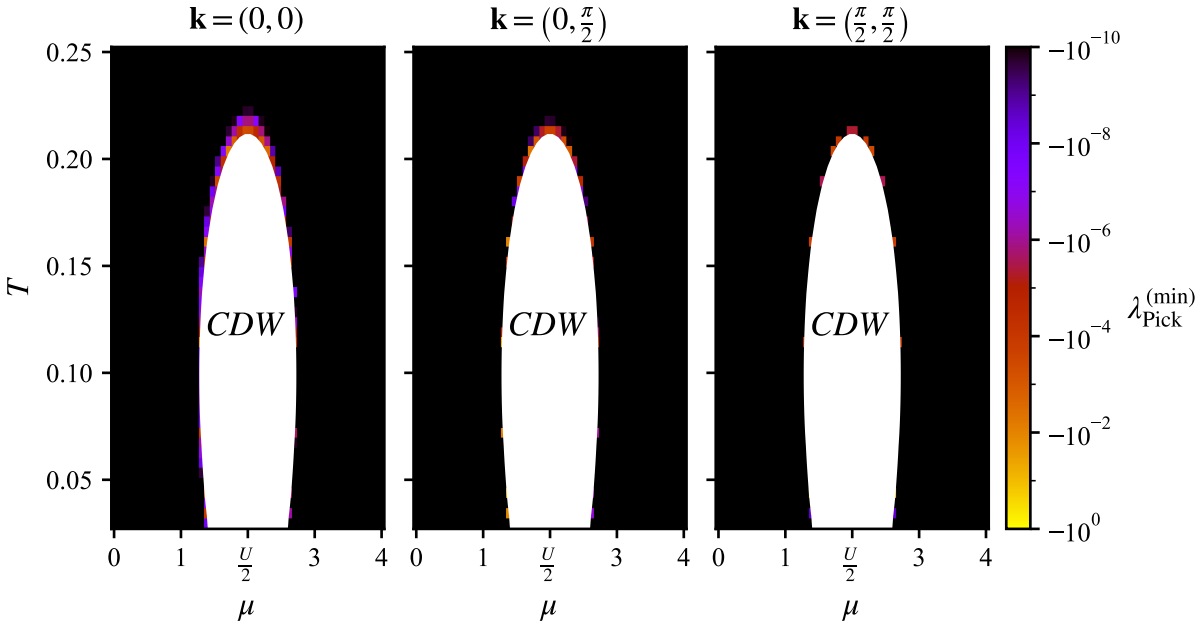

Figure 23: $T - \mu$ parameter-space diagram of the minimum Pick eigenvalues, $\lambda_{\text{Pick}}^{\text{min}}$, obtained from one-shot dual-fermion simulations for $L = 16$ at $U = 4$ using the full ladder resummation of the BSE. The white region marks the CDW phase.